Intensity dependence of high-order harmonic generation in ZnO

Xin-Qiang Wang, MingQing Liu, Lijuan Jia, Pei-Guang Yan, and Wei-Chao Jiang[*]

Institute of Quantum Precision Measurement, College of Physics and Optoelectronic Engineering,
Shenzhen University, Shenzhen 518060, China

The laser intensity dependence of high-order harmonic generation (HHG) in ZnO is investigated theoretically. We find that the intensities of lower-order harmonics mainly contributed by the intraband electron oscillation increase with light intensity monotonously. However, the intensities of higher-order harmonics where the interband electron-hole recollision dominates oscillate with light intensity. We build models of intraband and interband electronic dynamics to study the effect of laser intensity on every single-order harmonic that is far from the band gap. The model results are in good agreement with the numerical solution of semiconductor Bloch equations. The nonzero initial $\vec{k}$ positions play an important role in HHG, especially in higher-order harmonics. With the saddle-point method, the critical distance for electron-hole recombination in the current material and laser parameters is found to be one lattice constant in the dephasing time of a quarter of laser cycle. A unified description of channel closing effects is proposed to explain the laser intensity dependence of above threshold ionization and HHG in gases and solids including HHG not far from the band gap.

I. INTRODUCTION

High-order harmonic generation (HHG), as a major branch of strong-field physics, has been extended to interactions between lasers and solids [1,2] and liquids [3] from gases [4]. There are two important applications of HHG: One is to generate new ultrashort light sources [5], and the other is to detect structural [6–10] and dynamic information [5,11–13] of matter. HHG in solids has been extended from bulk semiconductors [1] to monolayer materials [14,15], tailored or engineered solid materials [16–18], Weyl semimetal β-WP$_2$ crystals [19], and topological insulators, including the model system of a linear chain of singly charged ions [20], Haldane model [21,22], and realistic three-dimensional topological insulator Bi$_2$Se$_3$ [23,24].

In all the laser-matter interaction processes, the effects of laser intensity and wavelength are very fundamental, as they are basic parameters of pulses. The laser intensity dependence of the cutoff energy of solid HHG has been experimentally studied in ZnO [1], solid Ar, and solid Kr [25]. The laser intensity dependence of single-order harmonic has been experimentally studied in ZnO [1,26], an Au nanoantenna array [17], 2-mm-thick ZnSe film (HHG near and below the band gap) [27], grating structures composed of thin Si ridges, and bulk Si [18]. However, the mechanism behind these phenomena remains to be studied. In the experimental results of ZnSe film, the intensities of HHG below the band gap increase monotonously with the light intensity in Fig. 3 of Ref. [27]. This phenomenon also occurs in Fig. 2 in the present study. An oscillation appears in the laser intensity dependence of the 15th-order harmonic in bulk Si in Fig. 4(d) of Ref. [18], which might be the footprint of the phenomena presented in Figs. 3

and 8(c) in our current work. But this phenomenon is not the focus of Ref. [18], and they did not explain it.

Some numerical and theoretical studies were performed in different materials and model potentials [28–30] with different theoretical methods. Different models were built to explain the intensity dependence of harmonics, for example, subcycle interferences between electrons pumped to the conduction band at different times [28], the contribution of Floquet-Bloch states [29], and quantum path interferences [30]. Since there are few experimental studies on laser intensity dependencies of solid HHG, especially for higher-order harmonics, and there are different theoretical explanations, it is very meaningful to conduct a more accurate and detailed theoretical study on the light intensity dependence of harmonics.

In Ref. [29], Jin *et al.* calculated HHG from one- and two-dimensional model potentials with the time-dependent Schrödinger equation (TDSE) with a single $\vec{k}$ point and the whole Brillouin zone as the initial state, respectively. It was found that the harmonic yield of the harmonic plateau region and the 11th-order harmonic oscillates with the light intensity. The Floquet-Bloch theory and the strong-field approximation were used in Ref. [29] to explain the oscillation of harmonics. The effect of multiple bands is naturally included in the calculation of TDSE with model potentials [29,31,32]. Higher-energy bands contribute to higher-harmonic plateaus. In moderate light intensities, the solid materials will not be damaged, and only the first harmonic plateau can be observed experimentally [1,26,33]. In these cases, the contribution of higher-energy bands can be ignored, which is the case in our current study. The complex solutions of the ionization saddle-point equation were obtained with approximations in Ref. [29]. In our current work, we find that although the ionization time determined by Eq. (24) is important, the ionization yield has little effect on the intensity dependence of HHG, so the band gap is disregarded in the ionization saddle-point equation, which is

---

*jiang.wei.chao@szu.edu.cn

helpful to give a semiclassical physical picture of the electron motion.

In Refs. [28,30], the semiconductor Bloch equation (SBE) was numerically solved to investigate the laser intensity dependence of HHG in ZnSe, solid Ar, ZnO [28], and MgO [30]. The oscillation of harmonic yield with the light intensity was explained by the interference of different ionization events around the adjacent pulse peaks separated by a half optical cycle [28] and the interference between short and long quantum paths [30]. In our present study, the intensity dependencies of different-order harmonics are obtained by the intraband model and the saddle-point method. It is found that the interference effect applicable to all oscillatory structures of intensity dependence curves is more complicated than that in Refs. [28,30]. The interference effects in the time domain are different in different light intensities. The interference between short quantum paths may produce a maximum or a minimum. A minimum value might come from the interference between short quantum paths or from the interference between short and long quantum paths.

In the calculations of TDSE and model theories, the case with $\vec{k} = 0$ as the initial state is usually considered as a main or representative part [28,29,31,34–36] to study the laser-material interaction even though the full Brillouin zone integration is performed in the same time with the TDSE [29,36] or SBE methods [28,29,31]. Beyond the single-active-electron approximation, the contribution of electron correlation to HHG is studied using time-dependent density-functional theory [37–39]. The importance of contributions of nonzero initial $\vec{k}$ points is discussed in Ref. [40] by comparing HHG calculated by TDSE and SBE in the same conditions. Crystal-momentum-resolved contributions to HHG have been studied in Refs. [36,41–44]. Electrons tunneling from regions away from the minimum band gap have been found to play an important role in the interaction between solids and elliptically polarized pulses [45]. However, whether and how much the initial state of $\vec{k} = 0$ contributes to HHG remains to be studied. All initial $\vec{k}$ positions in the valence band are taken into account in our study. We find that the point $\vec{k} = 0$ as the initial state may make a great contribution to the intraband harmonics, but it may make almost no contribution to the interband harmonics.

The light intensity dependence of the harmonic yield integrated over a wide range of frequencies has been studied in Refs. [28,29]. In our current work, harmonics far from the band gap will be studied separately according to the order. We extend the model of intraband electron oscillation to study harmonics below the band gap. We develop the model of interband electron-hole recombination with the saddle-point method to study the intensity dependence of each single-order harmonic above the band-gap region. With these more rigorous models, the electron dynamics behind a single-order harmonic can be found and disassembled in the energy-$\vec{k}$ space and in the real space. Different explanations of the intensity dependence of HHG can be checked. The phrase "far from the band gap" refers to spectral regions where either intraband or interband harmonic radiation dominates, and the interference between them can be ignored. However, the quantitative boundary value of the region where interference can

be ignored has not been determined yet, which needs further study.

The laser intensity dependencies of above threshold ionization (ATI) [46–49] and HHG [47,50,51] in gases have been studied. Resonance-like enhancements called channel-closing effects appear in the ATI and HHG spectra. However, this effect in solid HHG has not yet been confirmed through experimental observations. In Sec. III D, we have re-examined the intensity dependence of ATI and HHG in gases with TDSE and compared the results to those of solid HHG. Our findings indicate that the oscillations presented in the intensity dependence of solid HHG in our current study are due to a similar channel-closing effects, although there are some distinct differences in the properties of the oscillations between HHG in solids and ATI and HHG in gases. We established the connection between channel-closing effects in gases and solids by energy-band-structure-based images.

II. THEORETICAL METHODS

A. Semiconductor Bloch equations

The interaction process between ZnO and strong laser pulses is simulated by solving the SBE:

$$\frac{\partial}{\partial t}\xi_{2,1}(\vec{K}) = -\frac{\xi_{2,1}(\vec{K})}{T_d} + i\vec{F}(t) \cdot \vec{D}_{1,2}(\vec{K})$$
$$\times [n_{1,\vec{K}}(t) - n_{2,\vec{K}}(t)]e^{-iS_{2,1}(\vec{K},t)}, \quad (1a)$$

$$\frac{\partial}{\partial t}n_{m,\vec{K}} = s_m i\vec{F}(t) \cdot \vec{D}_{2,1}(\vec{K})\xi_{2,1}(\vec{K})e^{iS_{2,1}(\vec{K},t)} + \text{c.c.}, \quad (1b)$$

where $T_d = T_0/4$ is the dephasing time, T_0 is the period of the pulse, and n_m is the population of the mth band. The valence and conduction bands are marked with $m = 1$ and $m = 2$, respectively. $s_m(s_1 = 1, s_2 = -1)$ is a sign factor for unifying equations of different bands. The magnitude of the transition dipole $\vec{D}$ is denoted by D. D at Γ point is 3.46 [52]. The parameters of the one-dimensional (1D) band structure along the Γ-M direction provided in Ref. [53] are used in our calculations. k and K are the magnitudes of the quasimomentum $\vec{k}$ and $\vec{K}$, respectively. The electric field is linearly polarized along the Γ-M direction in ZnO. The pulse envelope

$$f_e(t) = \begin{cases} \sin^2\left[\frac{\pi}{2\tau_u}(t - t_0)\right], & t \in [t_0, t_0 + \tau_u] \\ 1, & t \in (t_0 + \tau_u, t_f - \tau_d) \\ \cos^2\left\{\frac{\pi}{2\tau_d}[t - (t_f - \tau_d)]\right\}, & t \in [t_f - \tau_d, t_f] \end{cases}$$
$$(2)$$

is trapezoidal-like, which allows the starting and end points of the pulse and its derivative to be exactly zero. The whole duration of the pulse $(t_f - t_0)$ is seven cycles with 2-cycle uphill $(\tau_u = 2T_0)$ and 2-cycle downhill $(\tau_d = 2T_0)$. The vector potential is defined as $\vec{A}(t) = f_e(t)\vec{F}_0/\omega_0 \sin(\omega_0 t)$, where F_0 and ω_0 are the amplitude and angular frequency of the laser, respectively. The electric field strength is $\vec{F}(t) = -d\vec{A}/dt$. Each cycle is discretized into $2^{10} \times 4$ time points. The convergence has been tested with $2^{10} \times 2$ points per cycle and $2^{10} \times 6$ points per cycle. Other variables and parameters are described in Appendix A. The initial state of ZnO is selected to be the whole valence band; 601 $\vec{k}$ points at equal intervals are sampled in the valence band for the initial states. The con-

vergence has been tested with 301 and 1001 $\vec{k}$ points. Atomic units are used throughout the paper unless stated otherwise.

Intra- and interband currents are, respectively, defined as

$$\vec{j}_{\text{ra}}(t) = \sum_m \int \vec{v}_m(\vec{K}) n_m(\vec{K}, t) \, d\vec{K} \qquad (3)$$

and

$$\vec{j}_{\text{er}}(t) = \sum_{m,n,m>n} \frac{d}{dt} \int \vec{\wp}_{m,n}(\vec{K}, t) \, d\vec{K}, \qquad (4)$$

where

$$\vec{\wp}_{m,n}(\vec{K}, t) = \vec{D}_{m,n}(\vec{K}) \xi_{m,n}(\vec{K}) e^{iS_{m,n}(\vec{K},t)} + \text{c.c.} \qquad (5)$$

is the polarization between the mth and nth bands, and

$$\vec{v}_m(\vec{K}) = \nabla_{\vec{K}} E_m(\vec{K}). \qquad (6)$$

The total current is

$$\vec{j}_{\text{total}}(t) = \vec{j}_{\text{ra}}(t) + \vec{j}_{\text{er}}(t). \qquad (7)$$

The harmonic spectrum $\Theta(\omega)$ is obtained from the modulus square of the Fourier transform of the current's time derivative [54–56], i.e.,

$$\Theta(\omega) = \left| \int \exp(-i\omega t) \frac{d}{dt} \vec{j}(t) dt \right|^2 = |\omega \vec{J}(\omega)|^2, \qquad (8)$$

where $\vec{J}(\omega) = \int \exp(-i\omega t) \vec{j}(t) dt$. The same letter without vector superscript is the modulus of the corresponding vector.

B. Model of intraband harmonic generation

The intraband electron oscillation has been used to qualitatively explain the harmonic cutoff position that increases linearly with the increase in electric field strength [1,57]. Usually, in the model of intraband harmonic generation, the initial state is set as $\vec{k} = 0$ and the electron is ionized at the peak of the electric field. The electron motion is governed by

$$\frac{d}{dt} \vec{K}(t) = -\vec{F}(t). \qquad (9)$$

The electron group velocity, namely Eq. (6), is used to calculate the current. However, some factors are difficult to be taken into consideration, for example,

(1) the influence of the initial $\vec{k}$ positions of electrons on the current,

(2) the effect of electrons ionized at different times on the current, and

(3) the electron population evolution.

Therefore, the model of intraband electron oscillation is difficult to quantitatively explain harmonic spectra.

We extend this model with the help of the saddle-point method. The assumptions are listed as follows:

(1) The whole valence band is set as the initial state. The current is obtained by integrating all initial positions $\vec{k}_0$ in the first Brillouin zone.

(2) Electrons are ionized only at $K = 2n\pi/a_0, n \in Z$ (the minimum band-gap position), where a_0 is the lattice constant, which is required by the saddle-point equation Eq. (23).

(3) Electrons are ionized every time they pass the point $K = 2n\pi/a_0, n \in Z$. Currents generated by multiple ionization events should be added together.

(4) For each ionization event, the number of electrons transiting to the conduction band, $\Delta n_2(\vec{k}_0, t_{\text{ion}})$, is calculated by a product factor of the electric field strength and transition dipole moment D at the ionization time, namely $\Delta n_2(\vec{k}_0, t_{\text{ion}}) = |F(t_{\text{ion}})|D, (K(t_{\text{ion}}) = 2n\pi/a_0, n \in Z)$, which is assumed based on the ionization part of Eqs. (11) and (12).

(5) The direction and trajectory of electrons are determined by Eqs. (6) and (9).

(6) The current is 0 before the electron being ionized.

For the numerical implementation, the procedure is presented as follows:

(1) 601 $\vec{k}$ points are sampled in the valence band in the first Brillouin zone uniformly.

(2) For each initial position $\vec{k}_0$, the $\vec{k}$ path can be calculated as $\vec{K}(t) = \vec{k}_0 + \vec{A}(t)$.

(3) Find all the minimum-gap positions in the closed interval $[\min[\vec{K}(t)], \max[\vec{K}(t)]]$, denoted by $k_{\Gamma,n}(n = 1, 2, 3, \dots)$ which can span across multiple Brillouin zones.

(4) Solve $K(t) = k_{\Gamma,m}$ to obtain all the solutions of ionization times $t_{\text{ion},n}$, where the subscripted symbol n denotes the nth ionization time. For one initial $\vec{k}_0$, either no solution or many solutions is possible.

(5) For every initial $\vec{k}_0$ and the nth ionization time $t_{\text{ion},n}$, $\vec{K}(t)$ is used to calculate the electron velocity with the gradient of conduction band, i.e., $\vec{v}(\vec{k}_0, t_{\text{ion},n}, t) = \nabla_{\vec{k}} E_c[\vec{K}(t)]$. Before the ionization time $t_{\text{ion},n}$, the velocity is set as zero, i.e., $v(\vec{k}_0, t_{\text{ion},n}, t \leqslant t_{\text{ion},n}) = 0$.

(6) The increase in conduction-band population in the nth ionization event is estimated as $\Delta n_2(\vec{k}_0, t_{\text{ion},n}) = |F(t_{\text{ion},n})|D, (K(t_{\text{ion},n}) = 2m\pi/a_0, m \in Z)$.

(7) The intraband current corresponding to $\vec{k}_0$ and the ionization time $t_{\text{ion},n}$ is $\vec{j}_{\text{ra}}(\vec{k}_0, t_{\text{ion},n}, t) = \vec{v}(\vec{k}_0, t_{\text{ion},n}, t) \Delta n_2(\vec{k}_0, t_{\text{ion},n})$.

(8) The total intraband current is $\vec{j}_{\text{ra}}(t) = \int \sum_n \vec{j}_{\text{ra}}(\vec{k}_0, t_{\text{ion},n}, t) d\vec{k}_0$, where the summation with respect to n corresponds to the accumulation of multiple ionization events, and the integration with respect to $\vec{k}_0$ includes the contributions of different initial positions.

(9) The intraband harmonic spectrum is obtained from the modulus square of the Fourier-transformed current's time derivative, i.e., $\Theta_{\text{ra}}(\omega) = |\int \exp(-i\omega t) \frac{d}{dt} \vec{j}_{\text{ra}}(t) dt|^2 = |\omega \vec{J}_{\text{ra}}(\omega)|^2$.

In the extended model, there are still some factors not taken into account as follows:

(1) The reduction of electron population in the conduction band caused by the electron-hole recollision is not considered.

(2) The depletion of electron population in the valence band is neglected.

There are some methods to remedy these deficiencies as follows:

(1) The electron population curves calculated by SBE can be used to consider the depletion of valence band electron population and the evolution of the conduction band population.

(2) The depletion of valence band electrons can be calculated by the ionization saddle points and their corresponding ionization probabilities.

(3) The reduction of electron population in the conduction band can be computed by the product of the electric field strength and the transition dipole moment at the recollision saddle points.

However, electrons starting from one $\vec{k}$ point or different $\vec{k}$ points contribute to different order harmonics. As there are many ionization and recollision saddle points, these compensation methods will greatly increase the complexity of the intraband model. We have pointed out the drawbacks of the intraband model we currently use and proposed remedies for them, but these patches or remedies are not employed in our calculations. They are only suggested to be employed when necessary. The ionization part rather than the complete expressions of Eqs. (11) and (12) for the population is used in the intraband model, with the hopeful expectation that the results of SBE can be reproduced with as few terms as possible, which helps us to capture the main clue to the problem. An exact expression for intraband harmonic generation with all terms related to ionization, propagation, and recombination needs further study.

C. Saddle-point method

In an appropriate range of laser parameters the Keldysh approximation $n_{1,\vec{K}}(t) - n_{2,\vec{K}}(t) \approx 1$ [52,58] is valid and can be used to decouple equations of ξ and n in Eq. (1). Analytic solutions of the decoupled equations can be obtained as follows:

$$\xi_{2,1}(\vec{K}, t) = \exp\left(-\frac{t}{T_d}\right) \int_{t_0}^{t} dt' \exp\left[\frac{t'}{T_d} - iS_{2,1}(\vec{K}, t')\right]$$
$$\times i\vec{F}(t') \cdot \vec{D}_{1,2}[\vec{K}(t')], \quad (10)$$

$$n_{m,\vec{K}}(t) = n_{m,\vec{K}}(t_0) + [y_m(t) + \text{c.c.}], \quad (11)$$

where t_0 is the initial time,

$$y_m(t) = -\int_{t_0}^{t} dt' s_m \vec{F}(t') \cdot \vec{D}_{2,1}[\vec{K}(t')]$$
$$\times \int_{t_0}^{t'} dt'' \exp\left[\frac{t'' - t'}{T_d} + iS_{2,1}(\vec{K}, t'', t')\right]$$
$$\times \vec{F}(t'') \cdot \vec{D}_{1,2}[\vec{K}(t'')], \quad (12)$$

and

$$S_{2,1}(\vec{K}, t'', t') = S_{2,1}(\vec{K}, t') - S_{2,1}(\vec{K}, t''), \quad (13)$$

where t'' is the electron ionization time and t' is the electron-hole recombination time. The impact of electron ionization, propagation, and electron-hole recombination on the evolution of electron and hole population has been described in Eq. (12) with $\vec{F}(t'') \cdot \vec{D}_{1,2}[\vec{K}(t'')]$, $\exp[\frac{t''-t'}{T_d} + iS_{2,1}(\vec{K}, t'', t')]$, and $\vec{F}(t') \cdot \vec{D}_{2,1}[\vec{K}(t')]$, respectively. The corresponding analytic solution in atoms has been given in Ref. [59]. Then the interband current can be calculated by Eq. (4), which results in

$$\vec{j}_{\text{er}}(t) = \vec{\mu}(t) + \text{c.c.}, \quad (14)$$

where

$$\vec{\mu}(t) = \int_{\text{BZ}} d\vec{k}\vec{D}_{2,1}\left\{-i\frac{1}{T_d} - G_{2,1}[\vec{K}(t)]\right\} \int_{t_0}^{t} dt' \exp\left(\frac{t'-t}{T_d}\right)$$
$$\times \exp[iS_{2,1}(\vec{K}, t', t)]\vec{F}(t') \cdot \vec{D}_{1,2}, \quad (15)$$

and

$$G_{2,1}(t) = E_2(t) - E_1(t). \quad (16)$$

BZ denotes the first Brillouin zone. D has been assumed to be a real number and to be independent of $\vec{K}$ and t in the step to get the interband current. Equation (15) can be interpreted as a sum of probability amplitudes [59] of the processes of the electron ionization at t', the electron traveling in solids from t' to t, and the electron-hole recombination at t. The term containing $-i/T_d$ will not be strictly eliminated in Eq. (14), but it only contributes to lower-order harmonics in the current laser parameters and material, which has been omitted in Refs. [52,53].

The harmonic spectrum corresponds to the Fourier transform of the current's time derivative,

$$\Theta_{\text{er}}(\omega) = |\omega\vec{J}_{\text{er}}(\omega)|^2, \quad (17)$$

where

$$\vec{J}_{\text{er}}(\omega) = \vec{I}_1(\omega) + \vec{I}_2(\omega), \quad (18)$$

$$\vec{I}_1(\omega) = \int_{t=-\infty}^{t=+\infty} dt e^{-i\omega t}\vec{\mu}(t)$$
$$= \int_{t=-\infty}^{t=+\infty} dt \int_{\text{BZ}} d\vec{k}\vec{D}_{2,1}\left\{-i\frac{1}{T_d} - G_{2,1}[\vec{K}(t)]\right\}$$
$$\times \exp[iS_{2,1}(\vec{K}, t) - i\omega t] \int_{t_0}^{t} dt' \exp\left(\frac{t'-t}{T_d}\right)$$
$$\times \exp[-iS_{2,1}(\vec{K}, t')]\vec{F}(t') \cdot \vec{D}_{1,2}, \quad (19)$$

and

$$\vec{I}_2(\omega) = \int_{t=-\infty}^{t=+\infty} dt e^{-i\omega t}\vec{\mu}^*(t)$$
$$= \int_{t=-\infty}^{t=+\infty} dt \int_{\text{BZ}} d\vec{k}\vec{D}_{2,1}\left\{i\frac{1}{T_d} - G_{2,1}[\vec{K}(t)]\right\}$$
$$\times \exp[-iS_{2,1}(\vec{K}, t) - i\omega t] \int_{t_0}^{t} dt' \exp\left(\frac{t'-t}{T_d}\right)$$
$$\times \exp[iS_{2,1}(\vec{K}, t')]\vec{F}(t') \cdot \vec{D}_{1,2}. \quad (20)$$

We can get six saddle-point equations from the three integrals over $\vec{k}$, t', and t in Eqs. (19) and (20). They are listed as follows:

(1) For the integral over t', the saddle-point equations are

$$\frac{d}{dt'}[\pm iS_{2,1}(\vec{K}, t')] = 0. \quad (21)$$

They lead to the equation of ionization times

$$E_2[\vec{K}(t')] - E_1[\vec{K}(t')] = 0. \quad (22)$$

The classical approximation of neglecting the band-gap energy [53,59] is used to get a real solution, which means

$$E_2[\vec{K}(t')] - E_{\text{gap}} - E_1[\vec{K}(t')] = 0. \quad (23)$$

This results in

$$K(t') = n\frac{2\pi}{a_0}, \quad n \in Z, \tag{24}$$

which determines the ionization times. The real solutions of t' in the ionization equation, Eq. (24), are helpful to build a semiclassical picture of the electronic motion for HHG.

(2) For the integral over t, the saddle-point equatons are

$$\frac{d}{dt}[iS_{2,1}(\vec{K}, t) - i\omega t] = 0, \tag{25}$$

generated from Eq. (19), and

$$\frac{d}{dt}[-iS_{2,1}(\vec{K}, t) - i\omega t] = 0, \tag{26}$$

generated from Eq. (20). The solution of Eq. (25) is

$$\omega_p = E_2[\vec{K}(t)] - E_1[\vec{K}(t)], \tag{27}$$

which means the interband electron-hole recollision contributes to the harmonic generation. The solution of Eq. (26) is

$$\omega_m = E_1[\vec{K}(t)] - E_2[\vec{K}(t)], \tag{28}$$

which is the negative frequency term generated in the Fourier transform that corresponds to ω_p.

(3) For the integral over $\vec{k}$, the saddle-point equations are

$$\pm i\frac{\partial}{\partial \vec{k}}S_{2,1}(\vec{K}, t', t) = 0. \tag{29}$$

They result in

$$\vec{r}_{1,\vec{K}}(t) - \vec{r}_{1,\vec{K}}(t') = \vec{r}_{2,\vec{K}}(t) - \vec{r}_{2,\vec{K}}(t'), \tag{30}$$

which means the real space recollision for the electron-hole pair born at the same location. Through numerical tests, we find that the saddle-point results are in good coincidence with the SBE results when the critical distance of electron-hole recombination is set as one lattice constant which is 5.32 a.u. in ZnO, which means

$$|\vec{r}_{1,\vec{K}}(t) - \vec{r}_{1,\vec{K}}(t') - [\vec{r}_{2,\vec{K}}(t) - \vec{r}_{2,\vec{K}}(t')]| < a_0. \tag{31}$$

This is reasonable because the wave packet is delocalized and can spread in the real space [60].

The contribution of each pair of saddle points and their sum can be calculated by the following formulas:

$$\vec{I}_1(\omega) \approx \sum_{t_s}\sum_{\vec{K}_s}\vec{D}_{2,1}\left(-i\frac{1}{T_d} - \omega\right)\exp\left[-t_s\left(\frac{1}{T_d} + i\omega\right)\right]$$
$$\times \sum_{t'_s}\exp\left(\frac{t'_s}{T_d}\right)\exp[iS_{2,1}(\vec{K}_s, t'_s, t_s)]\vec{F}(t'_s) \cdot \vec{D}_{1,2}$$
$$\times \mathcal{F}[f(t'_s)]\,\mathcal{F}[f(t_s)]\,\mathcal{F}[f(\vec{K}_s)], \tag{32}$$

and

$$\vec{I}_2(\omega) \approx \sum_{t_s}\sum_{\vec{K}_s}\vec{D}_{2,1}\left(i\frac{1}{T_d} - \omega\right)\exp\left[-t_s\left(\frac{1}{T_d} + i\omega\right)\right]$$
$$\times \sum_{t'_s}\exp\left(\frac{t'_s}{T_d}\right)\exp[-iS_{2,1}(\vec{K}_s, t'_s, t_s)]\vec{F}(t'_s) \cdot \vec{D}_{1,2}$$
$$\times \mathcal{F}[-f(t'_s)]\,\mathcal{F}[-f(t_s)]\,\mathcal{F}[-f(\vec{K}_s)], \tag{33}$$

where

$$\mathcal{F}(z) = i\sqrt{\frac{2\pi}{|z|}}\exp\left[-i\frac{\arg(z)}{2}\right], \tag{34}$$

$$f(t'_s) = -i\nabla^2_{t'}S_{2,1}(\vec{K}_s, t')|_{t'_s}, \tag{35}$$

$$f(t_s) = i\nabla^2_t S_{2,1}(\vec{K}_s, t)|_{t_s}, \tag{36}$$

and

$$f(\vec{K}_s) = i\nabla^2_{\vec{K}}S_{2,1}(\vec{K}, t', t_s)|_{\vec{K}_s}. \tag{37}$$

t'_s and t_s are the ionization-time and recollision-time saddle points, respectively. $\vec{K}_s$ requires that the relation between t'_s and t_s must satisfy Eq. (30). The $\arg(z)$ is the argument of z, and $\arg(z) \in [0, 2\pi)$ for the current saddle-point formula.

In the derivation of all the saddle-point equations, the term, $\exp(\frac{t'-t}{T_d})$, is not taken into the calculation of the first derivative in the present study, as it is not an oscillatory exponential function of t or t', which is the same as Eq. (5) of Ref. [52] but different from Eq. (7) of Ref. [53]. There have been some variants of saddle-point methods for solid HHG. For example, the saddle-point method proposed in Ref. [52] has been extended to include Berry connections, transition dipole phases, and electron-hole polarization energy at recollision in Ref. [60]. It has also been used to simulate the superposition of contributions from a series of Gaussian wave packets in Ref. [61]. When T_d is infinity, Eq. (14) in the current work will correspond to Eq. (1) of Ref. [60] and Eq. (1) of Ref. [61]. Different from the current mathematical formalism, Wannier states rather than Bloch states are used to describe the wave function of valence band electrons in the expansion of the time-dependent electronic wave function in Ref. [62]. The corresponding saddle-point equations in Ref. [62] can depict the ionization and recombination at different sites in real space.

III. RESULTS AND DISCUSSION

The harmonic spectra calculated by SBE at the same wavelength but for different laser intensities are shown in Figs. 1(a) and 1(b). The band gap is at $8.66\omega_0$, around which the intra- and interband harmonic spectra have comparable strength and the interference between intra- and interband processes may significantly modify each other [31]. Harmonics below the band gap are mainly contributed by the intraband electron oscillation, while harmonics above the band gap are mainly contributed by the interband electron-hole recombination [34,35,52]. The farther the harmonic frequency is from the band gap, the more dominant the contribution becomes from one of the two dynamic processes.

In both the lower-intensity [Fig. 1(a)] and higher-intensity results [Fig. 1(b)], the intensity of the third-order intraband
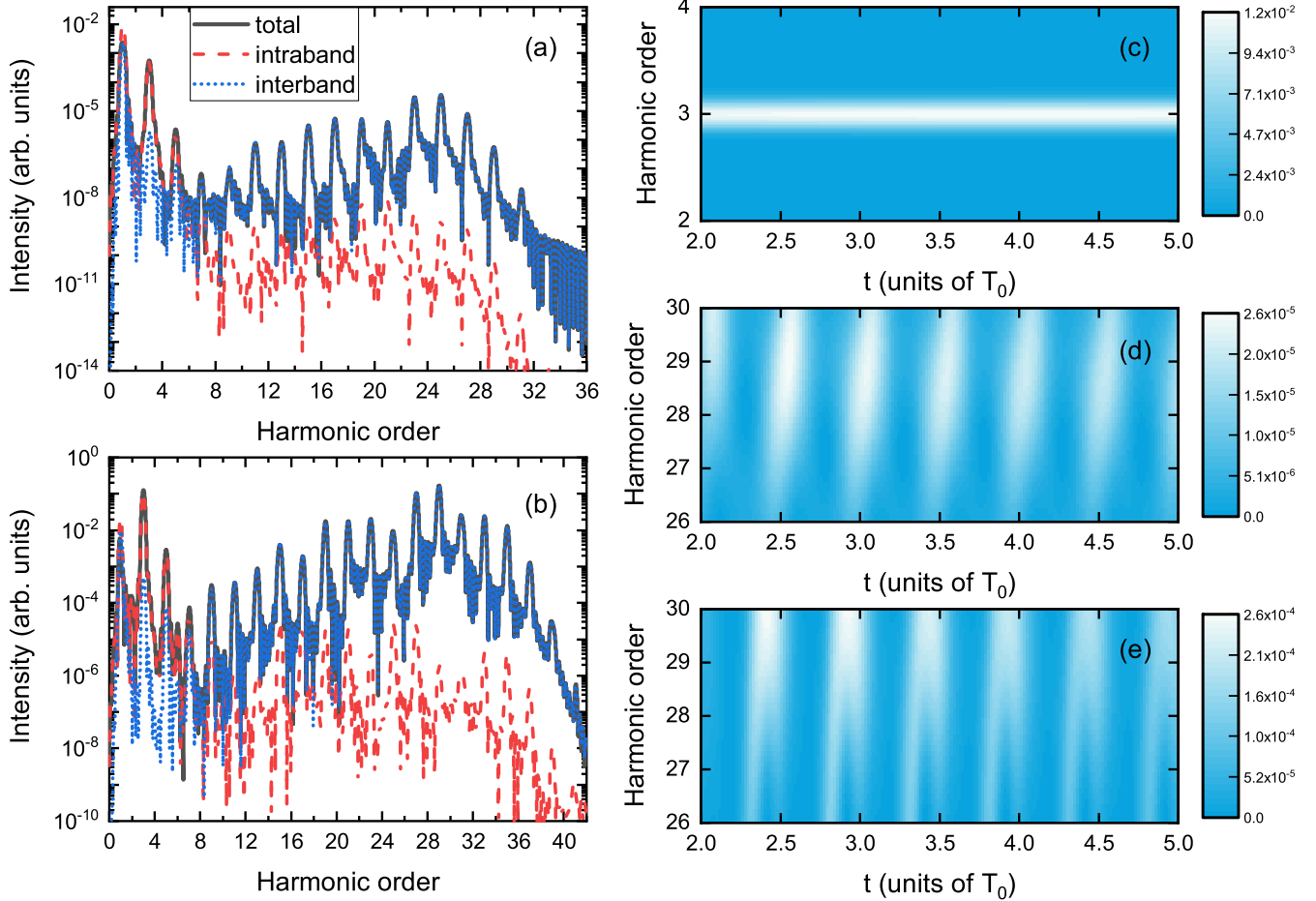
FIG. 1. Laser intensity dependence of high-order harmonic generation in ZnO. High-order harmonics are generated in ZnO at the intensities of (a) 3.1585×10^{11} W/cm^2 and (b) 2.246×10^{12} W/cm^2, respectively. The driving pulse wavelength is 3.2545 μm. The total (black solid line), intraband (red dashed line), and interband (blue dotted line) harmonic spectra are shown in (a) and (b). The time-frequency analysis is performed on the laser-induced total currents generated at [(c) and (d)] 1.3825×10^{12} W/cm^2 and (e) 1.8904×10^{12} W/cm^2. The time-frequency profiles of (c) low-frequency range and [(d) and (e)] high-frequency range are displayed separately.

harmonic is about three orders of magnitude larger than that of the interband harmonic. The difference between intensities of the intraband and interband harmonic spectra quickly reduces to nearly one order of magnitude at the fifth-order harmonic, which is shown in Figs. 1(a) and 1(b) and can also be seen in Fig. 2. In the above-band-gap frequency region in Figs. 1(a) and 1(b), the difference between intensities of the inter- and intraband spectra increases gradually with the harmonic order. The difference is about four orders of magnitude or even more in the cutoff region.

According to these phenomena, we will study the laser intensity dependence of lower-order harmonics that are dominated by the intraband electron oscillation with the intraband model developed in Sec. II B. The laser intensity dependence of higher-order harmonics that are dominated by the interband electron-hole recollision will be studied with the saddle-point method developed in Sec. II C.

Time-frequency analyses of different-order total harmonics in different laser intensities are shown in Figs. 1(c)–1(e). The third-order harmonic radiates at all times [Fig. 1(c)], which is the characteristic of intraband harmonic radiation. The radiation occurs at moments when the instantaneous electric

field is zero, which is due to two reasons. One reason is that the previously ionized electron has nonzero velocity and acceleration. The other reason is an inherent issue related to the principle of time-frequency analysis. The wavelet function used here is the Morlet wavelet [63],

$$\mathbf{w}(t_c, \omega, t) = \frac{\sqrt{\omega}}{\sqrt{\tau}} e^{i\omega(t-t_c)} e^{-(t-t_c)^2 \omega^2/(2\tau^2)}. \tag{38}$$

The wavelet function $\mathbf{w}$ contains a window function, given by $\exp[-(t-t_c)^2 \omega^2/(2\tau^2)]$, which is used to capture a segment of the time signal from the current. The complex oscillation function $\exp[i\omega(t-t_c)]$ is utilized for Fourier transform. The emission intensity at (t_c, ω) is the modulus square of

$$A(t_c, \omega) = \int j(t)\mathbf{w}(t_c, \omega, t)dt. \tag{39}$$

The time resolution is related to the cycle of the highest frequency to resolve. Because we can never extract an instantaneous time signal to perform Fourier transform, the emission intensity at the time moments when the electric field is zero cannot be resolved to be zero unless there is no radiation for a long period of time.
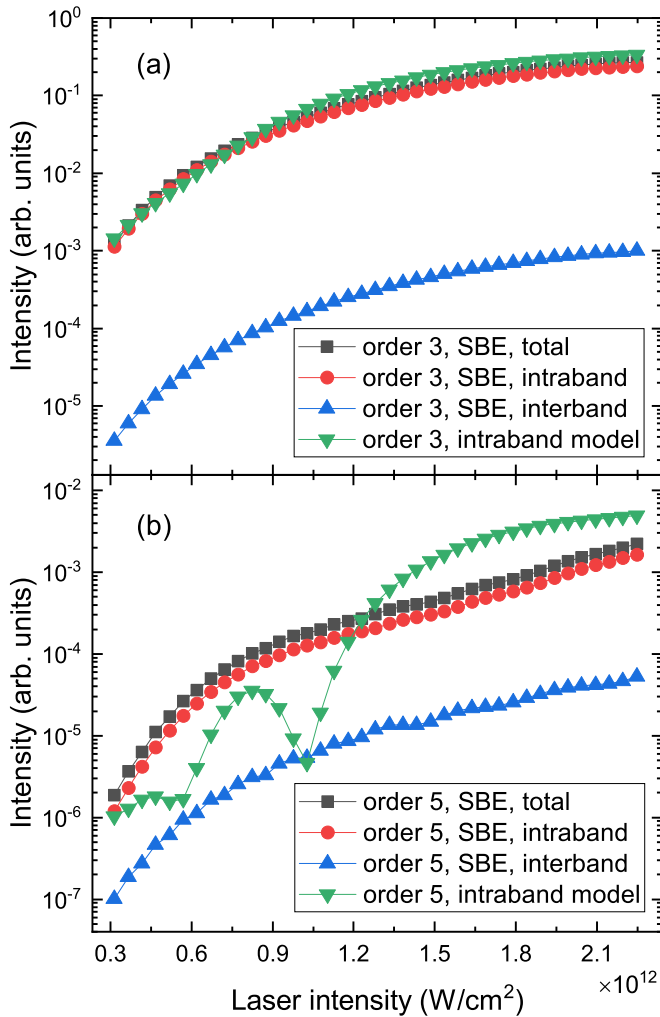
FIG. 2. Laser intensity dependence of low-frequency harmonics. (a) Intensity dependencies of the third-order total (blakc square), intraband (red circle), interband (blue upward triangle) harmonics and harmonics calculated by the model of intraband harmonic generation (green downward triangle). (b) is the same as (a) but for the fifth-order harmonic. For comparison, results from the intraband model are multiplied by 10^{-5}.

Short quantum paths appear in the radiation of higher-order harmonics [Fig. 1(d)], which is a signature of recollision. The contribution from long quantum paths at this laser intensity has attenuated because of the longer travel time. At a higher laser intensity, both short and long quantum paths contribute to the harmonic radiation, as is shown in Fig. 1(e). The occurrence time of radiation is earlier than that of lower laser intensity. These relatively pure intraband and interband radiations can be disassembled with our intraband model (Sec. II B) and saddle-point methods (Sec. II C), respectively.

A. Low-order region

The laser intensity dependence of any single-order harmonic is calculated by $|J(\omega)|^2$. The factor ω^2 in Θ is constant for a fixed frequency and thus has been discarded. The laser intensity dependencies of the third-order harmonic calculated by SBE and the intraband model are shown in Fig. 2(a).

With the increase in light intensity, the harmonic intensity increases monotonously. The intraband harmonics almost exactly reproduce the curve of the total harmonic radiation in the SBE results. The light intensity dependence of the third-order harmonic calculated by the intraband model is in good coincidence with the intraband and total spectra from SBE.

The intraband and the total harmonic spectra at the fifth order have a similar monotonous dependence on the laser intensity but have some differences in the harmonic intensity, as shown in Fig. 2(b). These differences between intraband and total harmonic radiation indicate that the interband contribution cannot be ignored. The radiation calculated by the intraband-model oscillates with the laser intensity, which can reproduce neither the intraband nor the total harmonic spectra. Because intensities of intraband and interband harmonics draw close to each other and their interference increases [31]. Frequent interband electron transitions make the evolution of electron population contributing to the fifth-order harmonic complicated. However, the intraband model cannot fully take into consideration the evolution of electron population and the interference between intraband and interband processes. So it is only applicable to low-order harmonics far from the band gap.

B. High-order region

The laser intensity dependencies of the 27th- and 29th-order harmonics are shown in Figs. 3(a) and 3(b), respectively. The harmonic intensities oscillate with the laser intensity, which is different from harmonics in the low-order region in Fig. 2. The agreement between the results of $n_1 - n_2 = 1$ (Keldysh approximation) and SBE verifies the accuracy of the Keldysh approximation. The results of saddle-point method also show corresponding oscillations in the intensity dependence curve, and the positions of peaks and valleys are in good agreement with SBE results, which verifies the accuracy of the saddle-point method. The saddle-point method retains the electron dynamic processes that make the main contribution. The maximum values of the saddle-point method increase more slowly with light intensity than SBE, which may be due to the approximation of the ionization process, as the classical approximation is made to transform Eq. (22) to Eq. (23). The minimum values remain almost unchanged with increasing intensity. This is because there is almost no noise background signal in the saddle-point method, so the sum of all saddle points near each minimum value approaches 0.

In order to find the electron dynamic processes behind the light intensity dependence, we extract the saddle points in the peaks and valleys for further analysis. The time-frequency analyses and saddle-point contributions of the 27th-order harmonic in different laser intensities marked by A, B, and C in Fig. 3(a) are shown in Fig. 4. In Fig. 4(a) only short quantum paths exist, which can be also checked in Fig. 1(d). The saddle points are plotted on the time-frequency analysis line according to recollision times. They are mainly distributed near the peaks and valleys of the time-frequency curve.

The saddle-point method is used to pick out the dynamic process which plays an important role in the final result from all the processes. Even if a dynamic process contributes a lot, if there is a corresponding comparable process to counteract it,
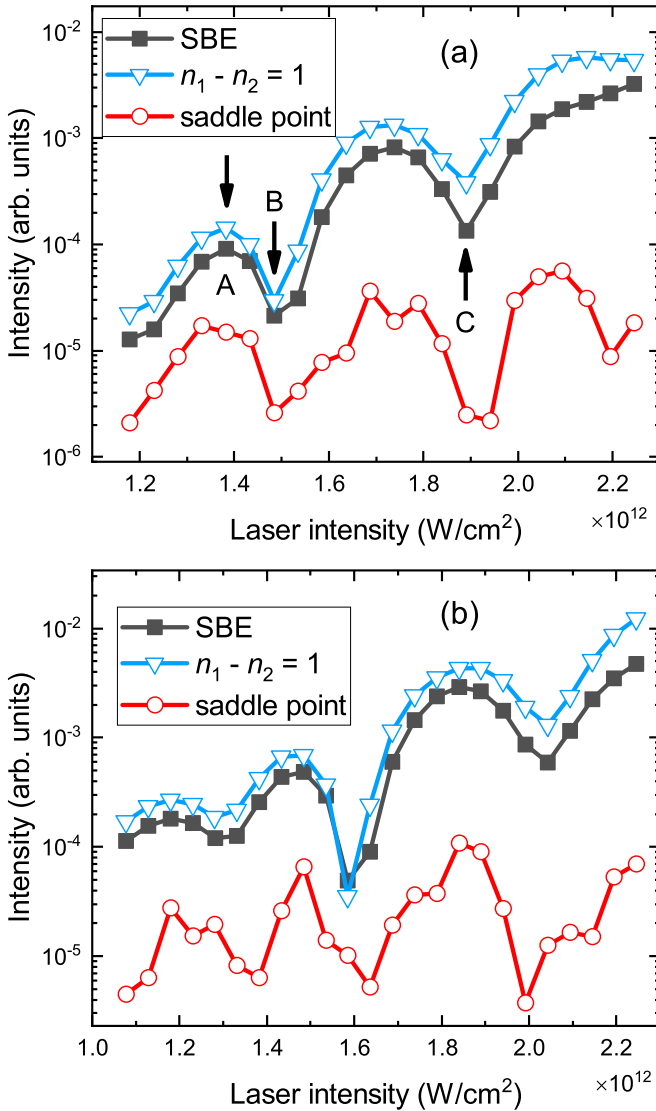
FIG. 3. Laser intensity dependence of high-frequency harmonics. (a) Intensity dependence of the 27th-order harmonic. The results calculated by SBE (black square), SBE with the Keldysh approximation $n_1 - n_2 = 1$ (blue downward triangle), and saddle-point method (red circle) are shown in (a). A, B, and C mark three extrema in the intensity dependence curve. Their intensities are 1.3825×10^{12} W/cm^2, 1.4841×10^{12} W/cm^2, and 1.8904×10^{12} W/cm^2, respectively. (b) The same as (a) but for the 29th-order harmonic. For visual clarity, the results from the saddle-point method are multiplied by 3×10^{-7}.

then neither of these two dynamic processes will be retained in the result of the saddle-point method. This leads to many zero-contribution regions on the time axis in the saddle-point results which correspond to the vacant regions in the line of saddle-point position in Fig. 4. Therefore, it is meaningless to directly show the intensity of each saddle-point contribution. A new sequence of points, namely the blue upward triangle points in Figs. 4(a) and 4(b), are set at the discrete positions on the time axis every 1/8 cycle. All contributions, $J_{er}(\omega)$, of saddle points within 1/32 cycle from each selected point are added together. The saddle-point contribution is consistent with the time-frequency analysis, which shows that the

saddle points localized in a small range of time can reflect the corresponding short-time dynamic process.

In Fig. 4(c), the saddle points are highly concentrated at the peaks and valleys of the time-frequency curve to form many saddle-point clusters. Recollision times of one cluster of saddle points are averaged to get the abscissa of one blue upward triangle point. The ordinate is the modulus of the sum of all complex amplitudes of saddle points in one cluster. The peaks and valleys can be well reproduced by the saddle-point contribution.

From the perspective of interference of quantum paths [30,64], both results in Figs. 4(a) and 4(b) are mainly formed by the interference of short paths. The interference of short quantum paths can result in both maximum and minimum radiations in the intensity dependence curve, as is shown in A and B in Fig. 3(a). There are both short and long quantum paths in Fig. 4(c), which can be also seen in Fig. 1(e). Then interferences between all short and long quantum paths play an important role in the minimum radiation of C in Fig. 3(a).

As the electron dynamics in solids are usually analyzed in the energy-$\vec{k}$ space, complex amplitudes of saddle points generated from the same initial $\vec{k}$ value are added together,

$$J_{er}(\vec{k}, \omega) = \sum_{t'_s, t_s, \vec{K}_s} J_{er}(\vec{k}, \omega, t'_s, t_s, \vec{K}_s), \tag{40}$$

to show a $\vec{k}$-resolved saddle-point contribution. The complex amplitudes, $J_{er}(\vec{k}, \omega)$, of different $\vec{k}$ values are drawn on the complex plane in Fig. 5. It is obvious that the sum of vectors in Fig. 5(a) will result in a larger vector, because the vector angles of most of them are concentrated in a narrow direction. The vectors in Fig. 5(b) counteract each other, because they point almost uniformly in all directions. The important information indicated by Fig. 5 is that harmonic radiations of electrons starting from different $\vec{k}$ points can be synchronized or asynchronized in different laser intensities. The sum of vectors can explain the maximum and minimum radiations in Fig. 3(a).

C. Discussion about electron dynamics

A classical approximation has been made to the saddle-point equation of electron ionization process in Eq. (22). It is necessary to discuss the validity of this approximation. The electron tunneling ionization process is partly disregarded with this approximation [53]. Therefore, the effect of ionization delay does not exist in our current saddle-point method. The accuracy of ionization yield might be decreased. However, a complete ionization process remains in the calculation results of SBE where this approximation is not made.

Since the results of electron ionization correspond to the change of electron population in different bands, we extract the evolution of electron population from SBE calculations to check whether the possible effect of light intensity on the ionization process plays a major role in the variation of harmonic radiation with the light intensity. The evolution of electron population with the light intensity and time is shown in Fig. 6. Although the electron population oscillates over time, as shown in Fig. 6(a), it does not oscillate with the light intensity, which can be seen in Fig. 6(b). In addition, the harmonics' oscillation with light intensity is not lost in the results
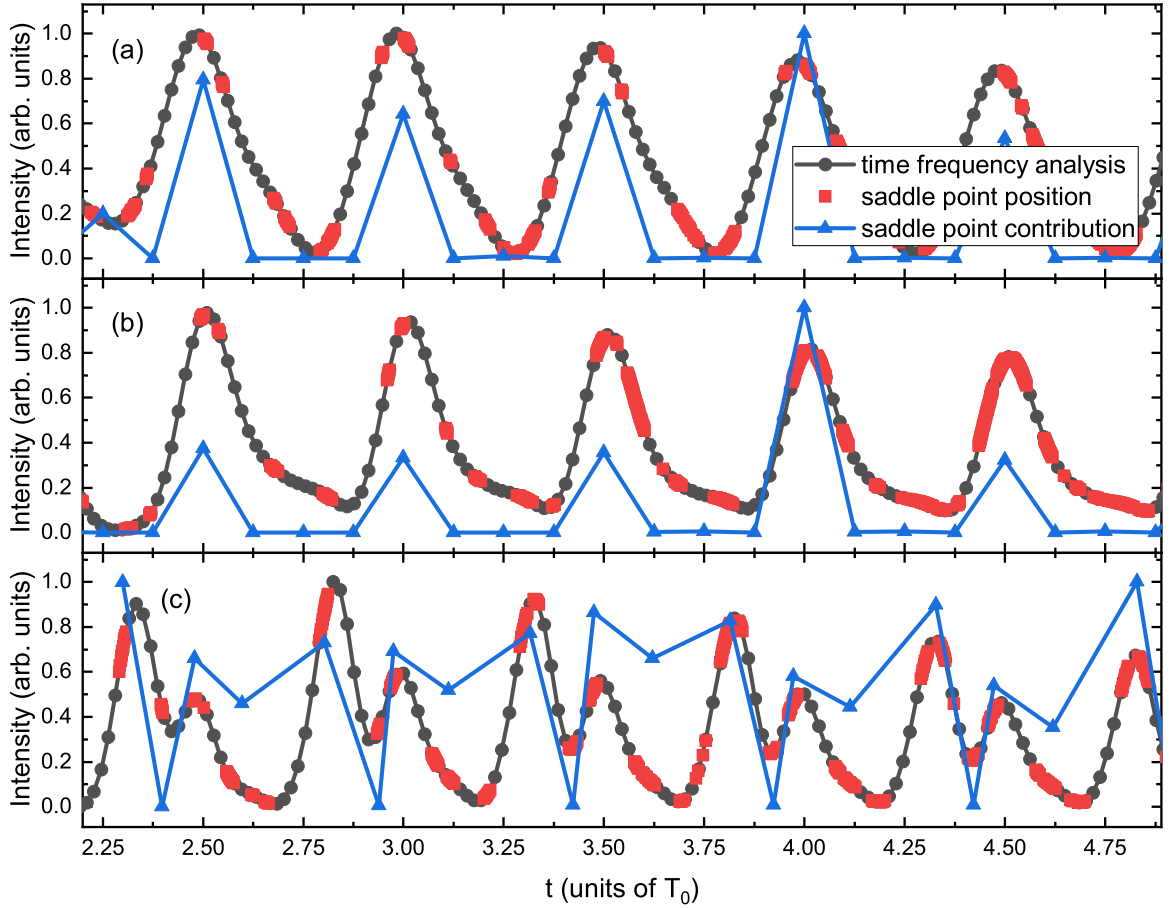
FIG. 4. Time-frequency analysis and saddle-point contribution of the 27th-order harmonic. The laser intensities of (a), (b), and (c) correspond to the intensities of points A, B, and C in Fig. 3(a). (a) The time-frequency analysis is performed on the total current calculated by SBE and is shown by the black dotted line. Saddle-point positions are marked by red squares. The saddle-point contribution is displayed by the blue upward triangle line. Panels (b) and (c) are the same as panel (a) but for different laser intensities.

of saddle-point method with this classical approximation for ionization, as shown in Fig. 3. Hence, the impact of electron ionization yield on the oscillation of harmonic radiation with light intensity is not evident, and this approximation for ionization is valid. However, the electron excitation probabilities may be different at different wavelengths [65] and in materials with different orientations and sizes [66]. In these cases, the influence of ionization process on the harmonic radiation may be reflected, which needs further study.

If we want to build a simple model for the electron dynamics, then some key points are necessary: Which initial state does the electron start from? What process does it go through? And what does it contribute to the final result? We extract the contribution of electrons starting from different $\vec{k}$ positions to harmonics. The corresponding results as a function of initial crystal momentum $\vec{k}$ are shown in Fig. 7. It can be seen from Fig. 7(a) that the radiation of the third-order harmonic that is mainly contributed by the intraband electron oscillation comes from a wide range of $\vec{k}$ points, of which the biggest contribution comes from $\vec{k} = 0$. However, the radiation of the 27th-order harmonic that is mainly contributed by the interband electron-hole recollision mainly comes from the trajectories whose initial $\vec{k}$ positions are far from zero, as shown in Fig. 7(b). Therefore, a model of electronic dynamics

with $\vec{k} = 0$ as the initial state may contain part of the intraband harmonic information, but it might be difficult to include the interband harmonic information.

The six key initial positions corresponding to the six peaks in Fig. 7(b) are discrete and symmetric with respect to $\vec{k} = 0$. This feature is easy to understand according to the saddle-point method. Because the electron motion is restricted by the saddle-point equations of t', t, and $\vec{K}$ simultaneously, the electron that makes the main contribution to a certain order harmonic can only recollide at the position limited by Eqs. (27) and (30), and it can only be ionized at positions limited by Eq. (24), then it can only come from some specific initial $\vec{k}$ position as long as the band structure and the external field are determined. This means not only that the full Brillouin zone integration is important for the final HHG spectrum in the TDSE and SBE methods but also that the source locations of the electrons that generate a specific order of harmonic are found.

D. A unified description of channel closing effects in gases and solids

To get a deep understanding of the laser intensity effects on gases and solids, we compare the dependencies of ATI in
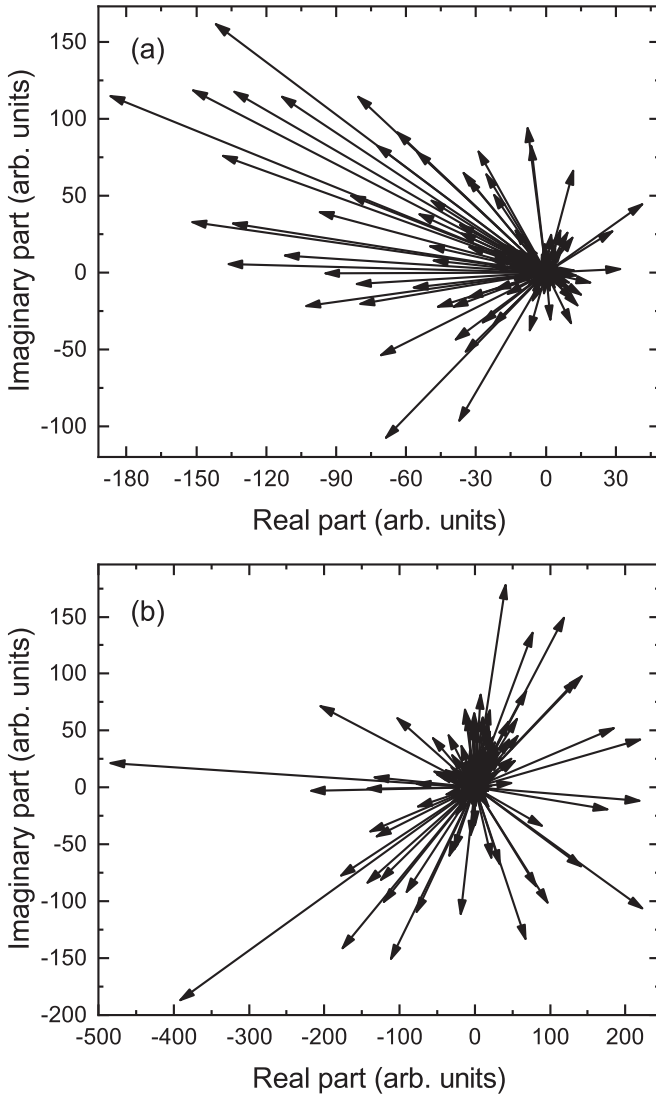
FIG. 5. Complex amplitudes of harmonic contribution from different $\vec{k}$ positions calculated by the saddle-point method. The laser intensities are (a) 1.3825×10^{12} W/cm^2 and (b) 1.8904×10^{12} W/cm^2, which corresponds to the intensities of points A and C in Fig. 3(a), respectively.
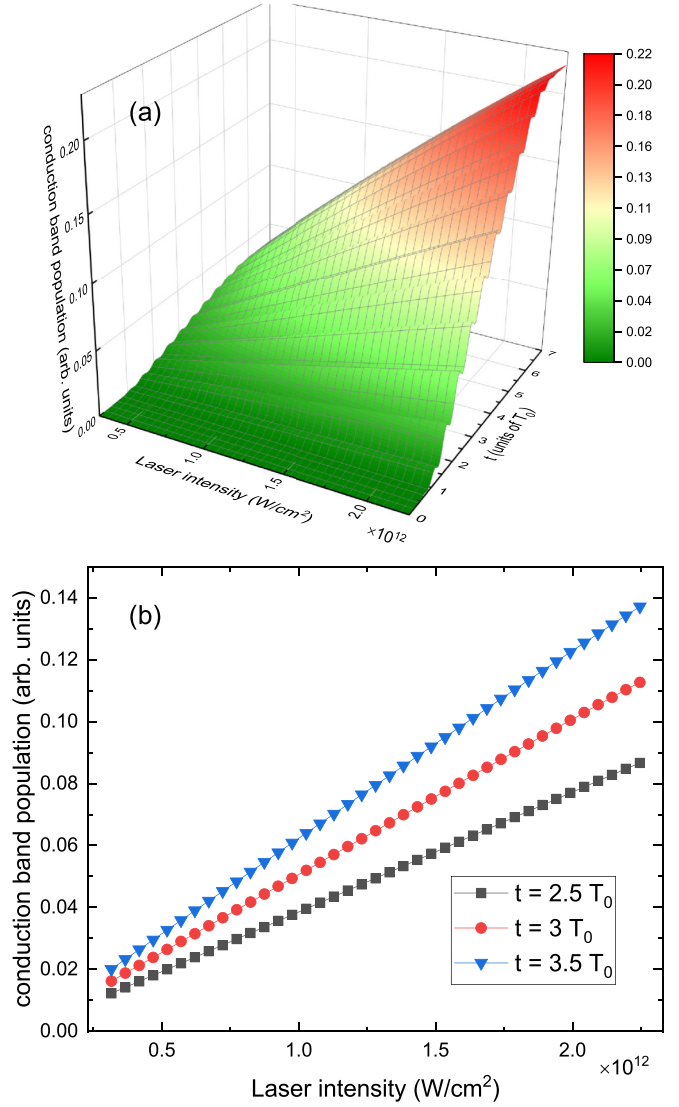

FIG. 6. Laser intensity dependencies of the electron population in the conduction band calculated by SBE. (a) Intensity and time dependencies of the electron population in the conduction band. (b) Intensity dependencies of the electron population at $2.5\,T_0$ (black square), $3\,T_0$ (red circle), and $3.5\,T_0$ (blue downward triangle). The curves in (b) are extracted from (a).

gases, and HHG in gases and solids, on light intensity. We find that although there are some different characteristics in the three spectra shown in Fig. 8, the laser intensity dependencies of ATI and HHG in gases and solids can be described in a similar way in the energy-band-structure picture.

The laser intensity dependencies of ATI in gases have been studied in Ref. [46] by TDSE, in Ref. [47] by a modified version of the strong-field approximation with one act of rescattering, and in Ref. [67] by a bicircular field. The kinetic energy of the ionized electron is

$$E \approx n\omega_0 - I_p - U_p, \tag{41}$$

where n is the number of photons absorbed by the electron, I_p is the ionization potential of hydrogen atom, and U_p is the ponderomotive potential,

$$U_p = \frac{I}{4\omega_0^2}. \tag{42}$$

We solve the 1D-TDSE numerically using the split wave-function method [68–70]. The electric field is $F_0 \sin(\omega_0 t) \sin(\pi t/t_p)^2$ with 5-cycle zero-value tail after the end t_p of the pulse with 20-cycle duration. The wavelength of the pulse is 630 nm; 3000 points are sampled per cycle. The coulomb potential of hydrogen atom is modeled by a soft-core potential $V(x) = -1/\sqrt{2 + x^2}$. The "internal zone" ends at 610 a.u. The "matching zone" starts at 130 a.u. The "external zone" in the calculation can reach 3584 a.u. The real space in the internal zone is discretized into 4896 points. The momentum space for external electrons is discretized into 22 564 points. The obtained laser intensity dependence of ATI
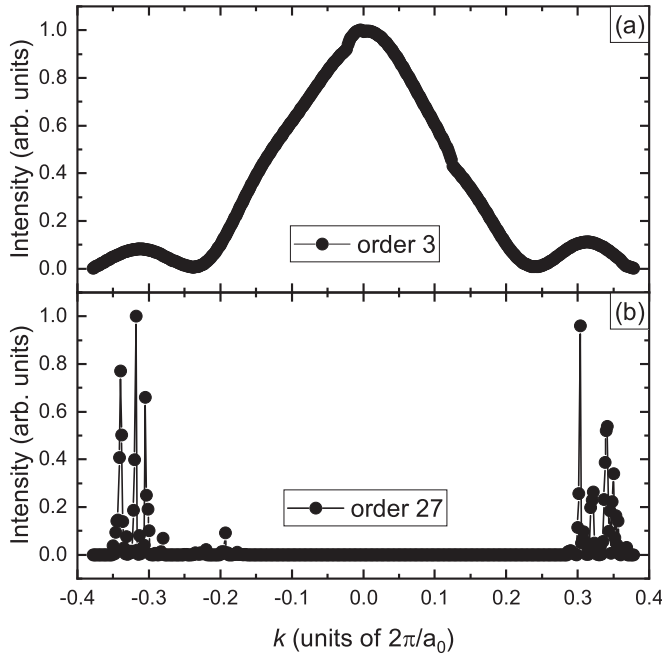
FIG. 7. Initial k resolved contribution to harmonic generation at the laser intensity of 1.3825×10^{12} W/cm^2 [corresponding to the intensity of point A in Fig. 3(a)]. (a) Contribution to the third-order harmonic calculated by the model of intraband harmonic generation. (b) Contribution to the 27th-order harmonic calculated by the saddle-point method.

spectra in the hydrogen atom is shown in Fig. 8(a). The ATI peaks shift to lower orders with the increase of laser intensity. This phenomenon can be well explained by the white dashed lines calculated by Eqs. (41) and (42).

For HHG in gases, the harmonic energy according to the three step model [71] is

$$E \approx I_p + \frac{p^2}{2} \xrightarrow{\text{cycle averaged}} E \approx I_p + U_p. \quad (43)$$

The laser intensity dependence of HHG in hydrogen is investigated by numerically solving the 1D-TDSE with an absorbing boundary function in the real space $[-300, 300]$ a.u. sampled with 2648 points. The pulse is the same as that defined in Sec. II A but with a wavelength of 800 nm. Each cycle is discretized into 4096 points for the time evolution. The HHG spectra are shown in Fig. 8(b). The harmonic peaks shift towards higher orders with the increase of light intensity. The dashed lines in Fig. 8(b) calculated by Eqs. (43) and (42) can well explain this phenomenon. By comparing Eqs. (41) and (43), we can see that the opposite slope of dependence of ATI and HHG on light intensity is due to the opposite sign before U_p.

The stripes of ATI and HHG spectra in gases shown in Figs. 8(a) and 8(b) are linear and uniformly distributed. However, significantly curved arc structures appear in the stripes of dependencies of solid HHG on light intensity in Fig. 8(c). Moreover, solid HHG spectra no longer oscillate with laser intensity in a uniform period, as shown in Figs. 8(c) and 3. At first glance, the intensity dependence of solid HHG appears to be significantly different from that of ATI and HHG in gases.
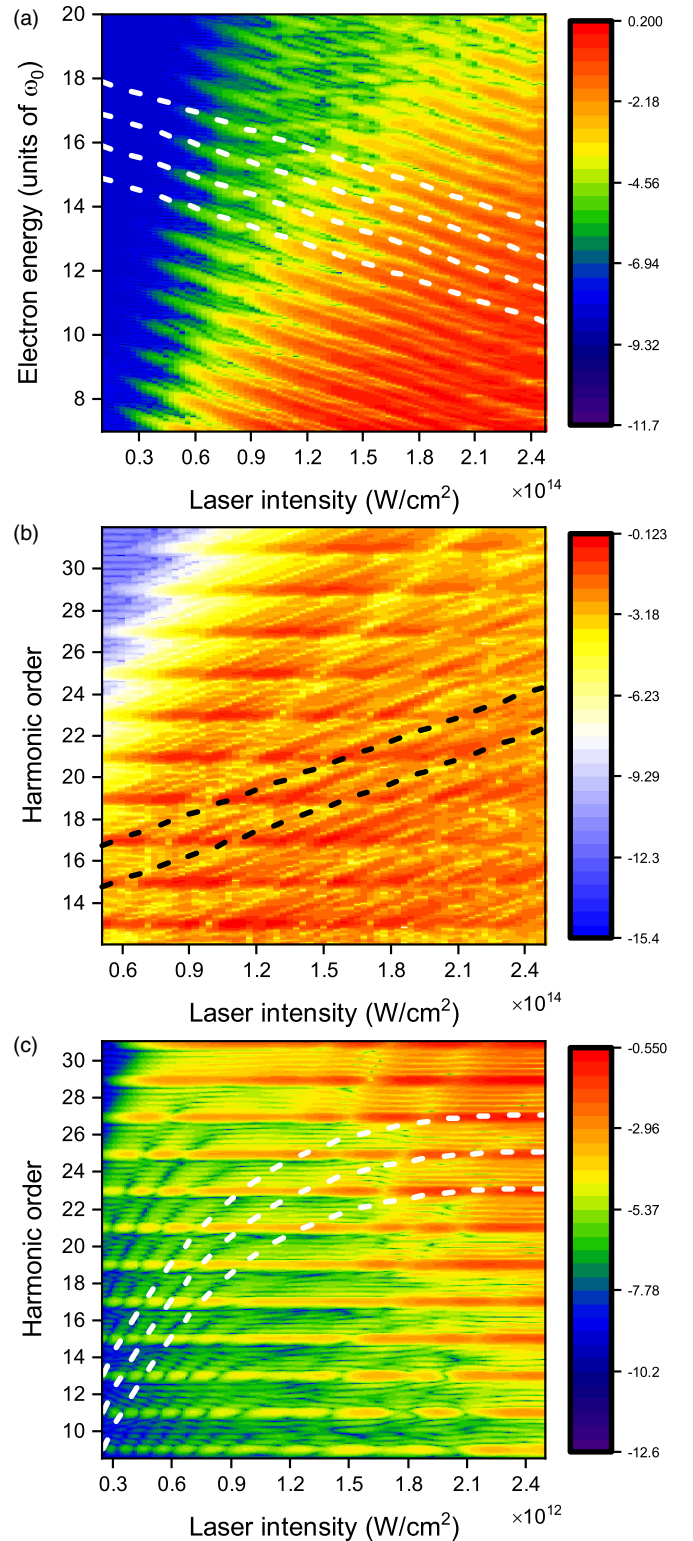

FIG. 8. Laser intensity dependencies of (a) ATI in hydrogen and HHG in (b) hydrogen and (c) ZnO. The z-axis data represented by color is logarithmic. The dashed lines in (a), (b), and (c) are calculated by the channel closing theories of ATI [Eq. (41)], HHG [Eq. (43)] in gases, and HHG in solids [Eqs. (50) and (51)], respectively. The dashed lines are separated by one photon energy in (a) and two photon energies in (b) and (c). Other lines translated from dashed lines are omitted to avoid obscuring the stripes on the color maps.
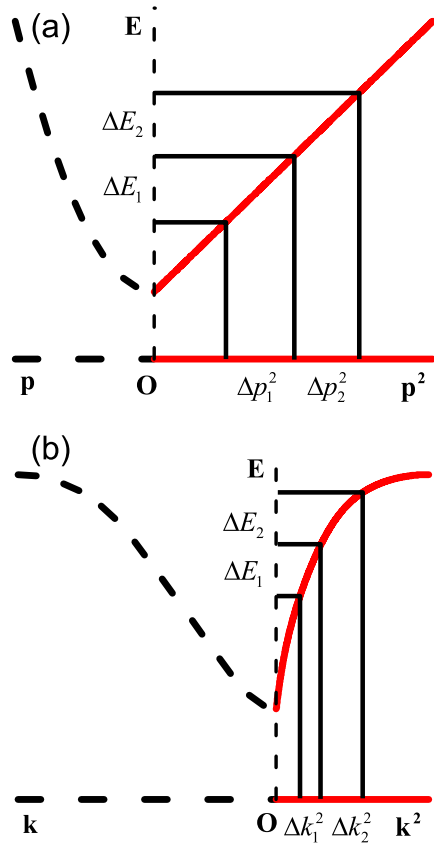
FIG. 9. Schematic diagram of channel closing effects in (a) gases and (b) solids. The coordinate axes are marked with the bold letters. (a) The free electron energy $p^2/2$ for the negative p and the ground-state energy are depicted by the black dashed lines. The lines of positive p are symmetric with the negative ones about the **OE** axis, so they are omitted in (a). The same energy curves are drawn in the p^2 axis with red solid lines in (a). ΔE and Δp^2 are the distances in the energy and p^2 axes. (b) The energy difference between the conduction and valence bands of ZnO is plotted in the k and k^2 axes. Other elements are similar to those in (a).

In addition, the channel closing effect is usually considered as a resonant ionization process in gases. As shown in Fig. 6, the electron population in ZnO does not exhibit oscillations with respect to light intensity, which appears to be in contrast to the channel closing effect observed in gases. However, we find that if the channel closing effect is considered as a process including ionization, propagation, and recollision (in HHG), then we can provide a unified explanation for the laser intensity dependence of ATI in gases and HHG in gases and solids by considering gas energy levels as energy bands.

The unified description of channel closing effects is shown in Fig. 9. It will be explained in detail in the following text. If we want to describe the electron dynamics on the field-free energy band structure, then the key is to establish the relation between laser parameters, electron motion and the horizontal and vertical coordinates of the energy band structure. For an ionized electron in gases, its kinetic energy follows the relation

$$E(p) = \frac{p^2}{2} \approx n\omega_0 - I_p - \frac{I}{4\omega_0^2}, \tag{44}$$

where $E(p)$ is the energy band on the p axis. There is a linear relation between p^2 and I in Eq. (44), which means

$$\Delta p^2 \propto \Delta I. \tag{45}$$

The slope of the $E(I)$ curve is $-1/(4\omega_0^2)$. Therefore, we can definitely see the effect of light intensity on the kinetic energy of ionized electrons directly in $E(p^2)$ function space.

The energy band structure of electrons in gases is shown in $E(p)$ and $E(p^2)$ spaces in Fig. 9(a). The parabola in the p axis becomes a straight line in the p^2 axis. $E(p^2)$ is linear on the p^2 axis, that is, if electrons absorb the same energy, then the required increase in light intensity is the same, which means

$$\Delta E_2 = \Delta E_1 \Rightarrow \Delta p_2^2 = \Delta p_1^2 \Rightarrow \Delta I_2 = \Delta I_1. \tag{46}$$

So ATI spectra vary linearly as a function of light intensity and the oscillation period remains constant, as shown in Fig. 8(a). For HHG in gases, there exist analogous relations and physical pictures, which can be also described in Fig. 9(a).

In solids, according to the acceleration theorem,

$$\frac{dk(t)}{dt} = -F(t) = -\sqrt{I} f_F(t), \tag{47}$$

where $f_F(t)$ is the t-dependent term. Because the time-dependent parts of $k(t)$ and $f_F(t)$ contain only the laser frequency and not the field strength, the derivative of $k(t)$ with respect to t does not generate a term that depends on laser intensity. Therefore, $k(t)$ is a linear function of $\sqrt{I}$, and

$$\Delta k \propto \Delta \sqrt{I}, \tag{48}$$

which is universal. To obtain the proportional coefficient between k and $\sqrt{I}$, we take the electric field of cosine form $F(t) = F_0 \cos(\omega_0 t + \varphi)$ as an example, since we are using a monochromatic pulse in this research. Integrating Eq. (47) yields:

$$k(t) = k(t_0) - \frac{\sqrt{I}}{\omega_0} \sin(\omega_0 t + \varphi). \tag{49}$$

The amplitude of $k(t)$ is

$$k_0 = \frac{\sqrt{I}}{\omega_0}, \tag{50}$$

with $k(t_0) = 0$. Therefore, the proportional coefficient between k and $\sqrt{I}$ is found to be $-1/\omega_0$. This establishes the relation between laser parameters, electron motion and the horizontal axis of energy band structure. The relation associated with the vertical axis E of energy band structure can be established based on the fact that the interband harmonic energy is determined by energy difference Eq. (27). The harmonic energy is

$$E = E_2(k^2) - E_1(k^2). \tag{51}$$

Therefore, the reason for the dependence of solid HHG on laser intensity can be found in $E(k^2)$ space, which has been drawn in Fig. 9(b). From Fig. 9(b), we can clearly see the following relation:

$$\Delta E_2 = \Delta E_1 \Rightarrow \Delta k_2^2 > \Delta k_1^2 \Rightarrow \Delta I_2 > \Delta I_1. \tag{52}$$

This is why the oscillation period of solid HHG increases with the light intensity, which has been shown in Figs. 3 and 8(c).

The dashed lines in Fig. 8(c) correspond to the minima of the spectra, which confirms the fact shown in Fig. 7(b) that the initial zero-k point has a small contribution to the interband harmonics.

IV. SUMMARY AND CONCLUSION

We have theoretically studied the laser intensity dependence of HHG in ZnO. We find that a large difference between intraband and interband harmonic spectra can exist in harmonics far from the band gap. In these regions, HHG is mainly contributed by either the intraband electron oscillation or the interband electron-hole recombination. The intraband harmonic radiation increases with the light intensity monotonously. The interband harmonic intensity oscillates with the light intensity. The model methods based on the intraband or the interband mechanisms can well explain the corresponding harmonic radiation.

For interband harmonics, the contribution of long quantum orbits is more likely to occur at high laser intensities. The electron ionization yield has little effect on the intensity-dependent oscillation of interband harmonic generation. Nonzero initial $\vec{k}$ points play an important role in HHG, especially in the interband harmonic radiation. The critical distance of electron-hole recombination is found to be nearly one lattice constant in the current material and laser parameters with the dephasing time of $T_d = T_0/4$. With this critical distance, the saddle-point results are in good agreement with the SBE results. When the dephasing time increases, a larger distance of electron-hole recombination might give contributions to harmonic radiation, because a longer dephasing time slows down the attenuation of electron and hole wave packets. Therefore, the critical distance of electron-hole recombination in the saddle-point method should be modified at different dephasing times.

A unified description of channel closing effects in gases and solids is proposed to explain the laser-intensity dependence of ATI and HHG in gases and solids. The unified theory can well explain the shift and extremum positions of ATI and interband HHG spectra, including almost all the interband HHG plateau. A small-enough step size of laser intensity maybe helpful to experimentally observe this laser-intensity-dependent oscillation and the curved arc stripes in solid HHG. The curved arc stripes in Fig. 8(c) can be seen as a measurement of the energy difference between valence and conduction bands. With the help of density-functional theory, the valence band can be obtained with high accuracy. Then an all-optical measurement of the conduction band can be performed with the measurement of laser intensity dependence of HHG.

The theoretical models can be used in multicolor pulses [13,43] and other materials including semimetals and semiconductors in the laser-solid interaction processes. As the saddle-point method contains the phase information of the electron dynamic process and harmonic radiation, it can be used to study various interference processes. The extension of our current saddle-point method with complete complex solutions [72,73] can be used to study the tunneling ionization process, which is expected to obtain the electron tunneling time in solids.

Further studies are needed to determine whether the effects presented in our current research also manifest in two or three-dimensional simulations, as well as in multiband simulations, other wavelengths, materials with nonparabolic bands, and after macroscopic propagation. The light intensity dependencies of electronic excitation processes in the cases of resonance in GaAs [74], valley polarization in graphene [65], and channel-closing effects in the Mathieu-type potential [32] have been studied, respectively. The specific embodiments of these electronic excitation effects in HHG need further study.

APPENDIX A: DERIVATION OF SBE FROM TDSE

The TDSE within the dipole approximation in the length gauge

$$i\frac{\partial}{\partial t}|\psi(t)\rangle = \left[\frac{\hat{\vec{p}}^2}{2} + V(\vec{r}) + \hat{\vec{r}} \cdot \vec{F}(t)\right]|\psi(t)\rangle \qquad (A1)$$

governs the laser-matter interaction process. In a periodic solid material, the time-dependent wave function can be assumed as the superposition of Bloch states,

$$|\psi(t)\rangle = \sum_n \int |\phi_{n,\vec{k}}\rangle c_{n,\vec{k}}(t) d^3\vec{k}, \qquad (A2)$$

where $\phi_{n,\vec{k}} = e^{i\vec{k}\cdot\vec{r}}u_{n,\vec{k}}$ is the Bloch state. Substituting Eq. (A2) into Eq. (A1), the equation of expansion coefficient can be obtained as follows:

$$i\frac{\partial}{\partial t}c_{m,\vec{k}'}(t) = \vec{F}(t) \cdot \sum_n \int \langle\phi_{m,\vec{k}'}|\hat{\vec{r}}|\phi_{n,\vec{k}}\rangle c_{n,\vec{k}}(t)d^3\vec{k}$$
$$+ E_{m,\vec{k}'}c_{m,\vec{k}'}(t). \qquad (A3)$$

With the relation of transition dipole [75]

$$\langle\phi_{m,\vec{k}'}|\hat{\vec{r}}|\phi_{n,\vec{k}}\rangle = -i\frac{\partial}{\partial\vec{k}}\delta_{m,n}\delta(\vec{k}-\vec{k}') + \delta(\vec{k}'-\vec{k})$$
$$\times \int d\vec{r}\langle u_{m,\vec{k}}|\vec{r}\rangle i\frac{\partial}{\partial\vec{k}}\langle\vec{r}|u_{n,\vec{k}}\rangle, \qquad (A4)$$

the coefficient equation, Eq. (A3), goes into the form

$$\frac{\partial}{\partial t}c_{m,\vec{k}}(t) = -iE_{m,\vec{k}}c_{m,\vec{k}}(t) - \vec{F}(t) \cdot \frac{\partial}{\partial\vec{k}}c_{m,\vec{k}}(t)$$
$$- i\vec{F}(t) \cdot \sum_n \int d\vec{r}\langle u_{m,\vec{k}}|\vec{r}\rangle i\frac{\partial}{\partial\vec{k}}\langle\vec{r}|u_{n,\vec{k}}\rangle c_{n,\vec{k}}(t).$$
$$(A5)$$

By introducing two transformations,

$$\vec{K}(t) = \vec{k} + \vec{A}(t), \qquad (A6a)$$

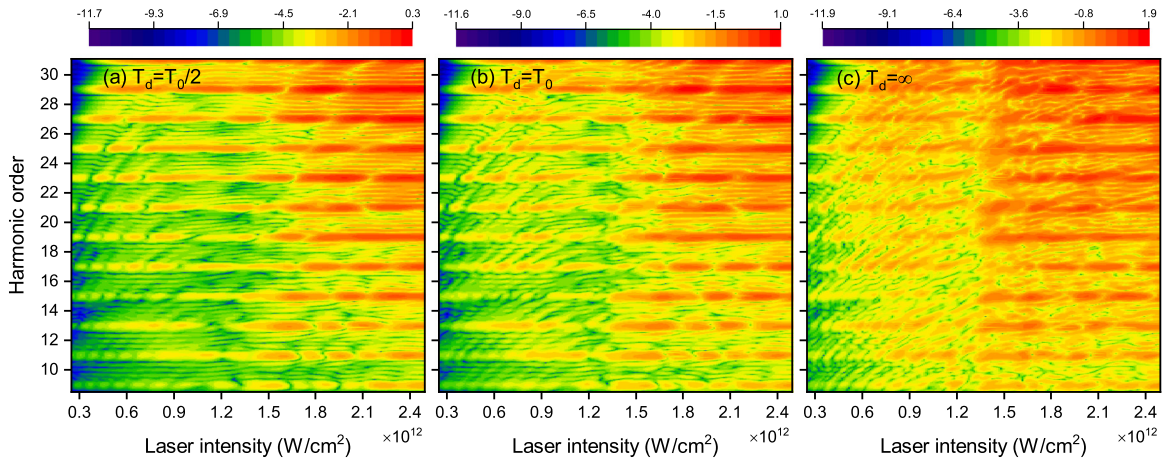$$c_{m,\vec{K}}(t) = b_{m,\vec{K}}(t)e^{-i\int_{-\infty}^t E_{m,\vec{K}}dt'}, \qquad (A6b)$$

FIG. 10. Effects of dephasing time. The laser intensity dependencies of HHG in ZnO with different dephasing times are shown in (a) $T_d = T_0/2$, (b) $T_d = T_0$, and (c) $T_d = \infty$. Other laser parameters are the same as those in Fig. 8(c).

terms about the derivative of c with respect to $\vec{k}$ and $E_{m,\vec{k}}c_{m,\vec{k}}(t)$ vanish. The equation of coefficient c, Eq. (A5), is transformed into the equation of b,

$$\frac{\partial}{\partial t}b_{m,\vec{K}}(t) = -i\vec{F}(t) \cdot \sum_n \vec{D}_{m,n}(\vec{K})b_{n,\vec{K}}(t)e^{iS_{m,n}(\vec{K},t)}, \quad \text{(A7)}$$

where

$$\vec{D}_{m,n}(\vec{K}) = \int d\vec{r}\langle u_{m,\vec{K}}|\vec{r}\rangle i\frac{\partial}{\partial \vec{K}}\langle \vec{r}|u_{n,\vec{K}}\rangle, \quad \text{(A8)}$$

and

$$S_{n,m}(\vec{K},t) = \int_{-\infty}^{t} E_n[\vec{K}(t')] - E_m[\vec{K}(t')]dt'. \quad \text{(A9)}$$

By introducing two new variables,

$$n_{m,\vec{K}} = b_{m,\vec{K}}^* b_{m,\vec{K}} \quad \text{(A10)}$$

and

$$\xi_{m,n}(\vec{K}) = b_{m,\vec{K}}^* b_{n,\vec{K}}, \ (m \neq n), \quad \text{(A11)}$$

and using their derivatives with respect to t and Eq. (A7), we get the two band density matrix equations Eq. (1). D has been assumed to be a real number in this step.

The derivation of SBE from TDSE is performed following the procedure given in Ref. [52]. In order to avoid the ambiguity of semantics and symbols, we give the derivation in Appendix A. Another reason for the derivation is that if we want to extend D to be complex numbers and k dependent, we need to know at which step D was approximated and what kind of approximation was made. In the current work, the transition dipole moment is not extended to be a complex and $\vec{k}$-dependent number. If D is a complex number and $\vec{k}$ dependent, then some additional terms, including the Berry connection and different forms of transition dipole moments, would arise in the SBE. The relation between transition dipole moments between different bands (for example, $D_{1,2}$ and $D_{2,1}^*$) will be dependent on the material symmetry [76]. The analytic solutions of the SBE and the saddle-point method would be more complicated. The $\vec{k}$-dependent transition dipole moment provided in Ref. [52] [Eq. (8) in the supplemental material]

is only a good approximation for small $\vec{k}$ around the Γ point. Therefore, the complex and $\vec{k}$-dependent transition dipole moment needs further study.

APPENDIX B: EFFECTS OF DEPHASING TIME

Since the dephasing time in the process of laser-material interaction remains undetermined, different dephasing times are tested to check the robustness of the laser intensity dependencies of HHG in ZnO discussed in the main text. Harmonic spectra in ZnO with different dephasing times are shown in Fig. 10. The harmonic intensity oscillation with light intensity and the curved arc stripes still exist in different dephasing times, even in the infinity dephasing time. However, as the dephasing time increases, the oscillation of the harmonic spectra may not be as clear as that under smaller dephasing times. Whatever the dephasing time is, it is still possible to observe this laser-intensity-dependent oscillation and the arc stripes.

APPENDIX C: SADDLE-POINT SIGNATURE OF HARMONIC RADIATION

There is a maximum value at $t = 4T_0$ in Fig. 4(b). The reasons for its occurrence are analyzed here. The readers will have a knowledge of what level of precision can be expected in different results. From the physical perspective, the population of electrons and holes is always evolving and not fixed. The amount of ionized electrons is influenced by the intensity of light and the number of electrons at the time of ionization. The electron population in the valence and conduction bands is not periodic in the time evolution, so the amount of ionized electrons varies in different laser cycles. In the earlier part of the pulse, there are fewer recollision times, but in the later part of the pulse, there are more recollision times, and the effect of multiple recollisions will be more pronounced in the later part. The multiple recollisions have different trajectories and periodicities, which disrupts the relatively good periodicity of the harmonic radiation caused by the first-recollision trajectories. The positions of saddle points are more scattered in the later part of the time axis than in the earlier part, as shown in Fig. 4(b). These reasons can cause the current and harmonic

radiation of a specific frequency to be physically nonperiodic. These nonperiodicities may be amplified in the saddle-point method.

From the mathematical perspective, the intensity dependencies of harmonics calculated by the saddle-point method have been shown in Fig. 3, which are in good agreement with the SBE results. In Fig. 3, the contributions from all initial k points and all saddle points at various ionization and recollision times have been summed together in the calculation of harmonic radiation intensity under a certain light intensity. Because the saddle-point method is a mathematical technique used to preserve the processes that make the main contribution to the final result in an integration, many processes that cancel each other out are not retained in the saddle-point method, which correspond to the blank spaces between the red points in Fig. 4. Therefore, we cannot expect that the time-resolved harmonic contribution obtained by the saddle-point method can reproduce the curve of time-frequency analysis at every time point. However, we want to check whether the saddle points finally retained can describe the main electronic dynamics information in a relatively short time range (locally near the peak and valley of the time-frequency analysis curve). For this reason, we uniformly select certain points (abscissas of the blue upward triangle points) near the peaks and valleys of the time-frequency curve. Then, we sum the contributions from the saddle points within a specific range centered around these sample points to obtain the ordinate of the blue points. This allows us to evaluate whether the saddle-point method can produce peaks and valleys in almost the same positions of the time-frequency curve. The selected interval range for summation may not encompass saddle points that have opposite phases. Therefore, the modulus of a single saddle-point contribution may be large due to the absence of corresponding cancellation terms.

Saddle points are mainly retained in some extremum positions of the integrand function and are generated at times with strong and weak radiation. Their amplitudes can differ significantly in magnitude. The distributions of the amplitudes and phases of the saddle points depend on the specific material and pulse. All the contributions of saddle points are calculated in detail and shown in Fig. 11(a) separately. The largest contribution around $t = 4T_0$ in Fig. 4(b) is found and marked with the red circle marker dashed line in Fig. 11(a). The red saddle point is found to originate from the initial position of $k = -0.3150 \times (2\pi/a_0)$. The k-resolved contributions of saddle points are shown in Fig. 11(b). The red saddle point comes from the initial position that makes the main contribution to the harmonic radiation, which is the saddle-point signature of harmonic radiation. In Fig. 11(a), the magnitude of the red saddle point exceeds 1300. Due to the introduction of saddle points ionized in the same position, the magnitude at $k = -0.3150 \times (2\pi/a_0)$ is reduced to be less than 1200 in Fig. 11(b). After summing up the saddle points within a range of 1/16 cycle, the peak intensity in Fig. 4(b) is reduced
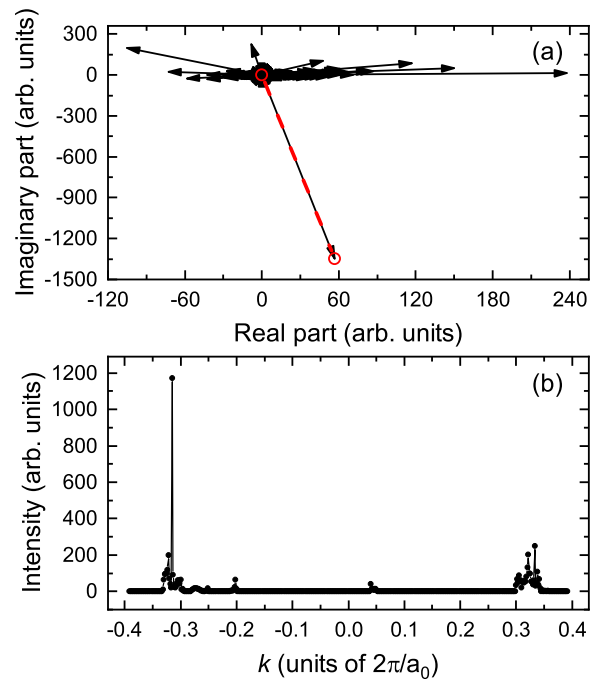

FIG. 11. Detailed analysis of saddle-point contributions at the laser intensity of 1.4841×10^{12} W/cm^2 [corresponding to the intensity of point B in Fig. 3(a)]. (a) The contributions of saddle points at different times of recollision are separately drawn on the complex plane. The red dashed line with circles as the initial and end points marks the largest amplitude of saddle-point contributions near the recollision time of $t = 4T_0$. (b) The initial-k-resolved contributions of saddle points.

to be nearly twice the magnitude of other cycles. When all the saddle points are summed together, a minimum radiation value appears in the laser intensity curve at point B in Fig. 3(a), which is experimentally measurable and consistent with the SBE results. All these results are physically and mathematically self-consistent.

Therefore, the amplitude of the blue triangle line in Fig. 4 is influenced by the physical nonperiodicity, multiple recollisions, the inherent issue of the saddle-point method, the approximation made in the solution of saddle-point equations, and the range of the summation interval in the time axis. The radiation decay caused by the dephasing time has been included in the saddle-point method. What we expect is for the saddle-point method to generate extremum values at approximately the same positions as the time-frequency curve. In Fig. 4(b), the peak value of saddle-point contributions near $t = 4T_0$ is about twice the magnitude of the saddle-point contributions in other cycles, which we think is reasonable, and even a larger difference is acceptable. The present results are good enough to show that the saddle-point method can capture the short-time-range dynamics information near the peaks and valleys of the time-frequency curve.

[1] S. Ghimire, A. D. DiChiara, E. Sistrunk, P. Agostini, L. F. DiMauro, and D. A. Reis, Observation of high-order harmonic generation in a bulk crystal, Nat. Phys. **7**, 138 (2011).

[2] S. Ghimire and D. A. Reis, High-harmonic generation from solids, Nat. Phys. **15**, 10 (2019).

[3] T. T. Luu, Z. Yin, A. Jain, T. Gaumnitz, Y. Pertot, J. Ma, and H. J. Wörner, Extreme-ultraviolet high-harmonic generation in liquids, Nat. Commun. **9**, 3723 (2018).

[4] R. Weissenbilder, S. Carlström, L. Rego, C. Guo, C. M. Heyl, P. Smorenburg, E. Constant, C. L. Arnold, and A. LHuillier, How to optimize high-order harmonic generation in gases, Nat. Rev. Phys. **4**, 713 (2022).

[5] J. Li, J. Lu, A. Chew, S. Han, J. Li, Y. Wu, H. Wang, S. Ghimire, and Z. Chang, Attosecond science based on high harmonic generation from gases and solids, Nat. Commun. **11**, 1 (2020).

[6] M. Lein, N. Hay, R. Velotta, J. P. Marangos, and P. L. Knight, Role of the Intramolecular Phase in High-Harmonic Generation, Phys. Rev. Lett. **88**, 183903 (2002).

[7] J. Itatani, J. Levesque, D. Zeidler, H. Niikura, H. Pépin, J. C. Kieffer, P. B. Corkum, and D. M. Villeneuve, Tomographic imaging of molecular orbitals, Nature (Lond.) **432**, 867 (2004).

[8] G. Vampa, T. J. Hammond, N. Thiré, B. E. Schmidt, F. Légaré, C. R. McDonald, T. Brabec, D. D. Klug, and P. B. Corkum, All-Optical Reconstruction of Crystal Band Structure, Phys. Rev. Lett. **115**, 193603 (2015).

[9] Y. S. You, D. A. Reis, and S. Ghimire, Anisotropic high-harmonic generation in bulk crystals, Nat. Phys. **13**, 345 (2017).

[10] L. Li, Y. Zhang, P. Lan, T. Huang, X. Zhu, C. Zhai, K. Yang, L. He, Q. Zhang, W. Cao, and P. Lu, Dynamic Core Polarization in High Harmonic Generation from Solids: The Example of Mgo Crystals, Phys. Rev. Lett. **126**, 187401 (2021).

[11] H. Niikura, F. Légaré, R. Hasbani, A. D. Bandrauk, M. Y. Ivanov, D. M. Villeneuve, and P. B. Corkum, Sub-laser-cycle electron pulses for probing molecular dynamics, Nature (London) **417**, 917 (2002).

[12] M. Lein, Attosecond Probing of Vibrational Dynamics with High-Harmonic Generation, Phys. Rev. Lett. **94**, 053004 (2005).

[13] Y. Lang, Z. Peng, J. Liu, Z. Zhao, and S. Ghimire, Proposal for High-Energy Cutoff Extension of Optical Harmonics of Solid Materials Using the Example of a One-Dimensional ZnO Crystal, Phys. Rev. Lett. **129**, 167402 (2022).

[14] N. Yoshikawa, T. Tamaya, and K. Tanaka, High-harmonic generation in graphene enhanced by elliptically polarized light excitation, Science **356**, 736 (2017).

[15] H. Liu, Y. Li, Y. S. You, S. Ghimire, T. F. Heinz, and D. A. Reis, High-harmonic generation from an atomically thin semiconductor, Nat. Phys. **13**, 262 (2017).

[16] M. Sivis, M. Taucer, G. Vampa, K. Johnston, A. Staudte, A. Y. Naumov, D. Villeneuve, C. Ropers, and P. Corkum, Tailored semiconductors for high-harmonic optoelectronics, Science **357**, 303 (2017).

[17] G. Vampa, B. G. Ghamsari, S. Siadat Mousavi, T. J. Hammond, A. Olivieri, E. Lisicka-Skrek, A. Y. Naumov, D. M. Villeneuve, A. Staudte, P. Berini, and P. B. Corkum, Plasmon-enhanced high-harmonic generation from silicon, Nat. Phys. **13**, 659 (2017).

[18] H. Liu, G. Vampa, J. L. Zhang, Y. Shi, S. Buddhiraju, S. Fan, J. Vuckovic, P. H. Bucksbaum, and D. A. Reis, Beating absorption in solid-state high harmonics, Commun. Phys. **3**, 192 (2020).

[19] Y.-Y. Lv, J. Xu, S. Han, C. Zhang, Y. Han, J. Zhou, S.-H. Yao, X.-P. Liu, M.-H. Lu, H. Weng, Z. Xie, Y. B. Chen, J. Hu, Y.-F.

Chen, and S. Zhu, High-harmonic generation in weyl semimetal β-wp$_2$ crystals, Nat. Commun. **12**, 6437 (2021).

[20] D. Bauer and K. K. Hansen, High-Harmonic Generation in Solids with and Without Topological Edge States, Phys. Rev. Lett. **120**, 177401 (2018).

[21] R. E. F. Silva, A. Jiménez-Galán, B. Amorim, O. Smirnova, and M. Ivanov, Topological strong-field physics on sub-laser-cycle timescale, Nat. Photon. **13**, 849 (2019).

[22] A. Chacón, D. Kim, W. Zhu, S. P. Kelly, A. Dauphin, E. Pisanty, A. S. Maxwell, A. Picón, M. F. Ciappina, D. E. Kim, C. Ticknor, A. Saxena, and M. Lewenstein, Circular dichroism in higher-order harmonic generation: Heralding topological phases and transitions in chern insulators, Phys. Rev. B **102**, 134115 (2020).

[23] D. Baykusheva, A. Chacón, D. Kim, D. E. Kim, D. A. Reis, and S. Ghimire, Strong-field physics in three-dimensional topological insulators, Phys. Rev. A **103**, 023101 (2021).

[24] D. Baykusheva, A. Chacón, J. Lu, T. P. Bailey, J. A. Sobota, H. Soifer, P. S. Kirchmann, C. Rotundu, C. Uher, T. F. Heinz, D. A. Reis, and S. Ghimire, All-optical probe of three-dimensional topological insulators based on high-harmonic generation by circularly polarized laser fields, Nano Lett. **21**, 8970 (2021).

[25] G. Ndabashimiye, S. Ghimire, M. Wu, D. A. Browne, K. J. Schafer, M. B. Gaarde, and D. A. Reis, Solid-state harmonics beyond the atomic limit, Nature (London) **534**, 520 (2016).

[26] S. Ghimire, A. D. DiChiara, E. Sistrunk, U. B. Szafruga, P. Agostini, L. F. DiMauro, and D. A. Reis, Redshift in the Optical Absorption of ZnO Single Crystals in the Presence of an Intense Midinfrared Laser Field, Phys. Rev. Lett. **107**, 167407 (2011).

[27] A. A. Lanin, E. A. Stepanov, A. B. Fedotov, and A. M. Zheltikov, Mapping the electron band structure by intraband high-harmonic generation in solids, Optica **4**, 516 (2017).

[28] T.-Y. Du, D. Tang, and X.-B. Bian, Subcycle interference in high-order harmonic generation from solids, Phys. Rev. A **98**, 063416 (2018).

[29] J.-Z. Jin, H. Liang, X.-R. Xiao, M.-X. Wang, S.-G. Chen, X.-Y. Wu, Q. Gong, and L.-Y. Peng, Contribution of floquet-bloch states to high-order harmonic generation in solids, Phys. Rev. A **100**, 013412 (2019).

[30] T.-J. Shao, L.-J. Lü, J.-Q. Liu, and X.-B. Bian, Quantum path interferences and selection in interband solid high-order harmonic generation in mgo crystals, Phys. Rev. A **101**, 053421 (2020).

[31] X.-Q. Wang, Y. Xu, X.-H. Huang, and X.-B. Bian, Interference between inter- and intraband currents in high-order harmonic generation in solids, Phys. Rev. A **98**, 023427 (2018).

[32] J. Li, L. Li, Q. Zhang, X. Zhu, T. Huang, P. Lan, and P. Lu, Channel-closing effects of electronic excitation in solids, Opt. Express **27**, 37224 (2019).

[33] Z. Wang, H. Park, Y. H. Lai, J. Xu, C. I. Blaga, F. Yang, P. Agostini, and L. F. DiMauro, The roles of photo-carrier doping and driving wavelength in high harmonic generation from a semiconductor, Nat. Commun. **8**, 1686 (2017).

[34] M. Wu, S. Ghimire, D. A. Reis, K. J. Schafer, and M. B. Gaarde, High-harmonic generation from bloch electrons in solids, Phys. Rev. A **91**, 043839 (2015).

[35] Z. Guan, X.-X. Zhou, and X.-B. Bian, High-order-harmonic generation from periodic potentials driven by few-cycle laser pulses, Phys. Rev. A **93**, 033852 (2016).

[36] F. Navarrete, M. F. Ciappina, and U. Thumm, Crystal-momentum-resolved contributions to high-order harmonic generation in solids, Phys. Rev. A **100**, 033405 (2019).

[37] N. Tancogne-Dejean, O. D. Mücke, F. X. Kärtner, and A. Rubio, Impact of the Electronic Band Structure in High-Harmonic Generation Spectra of Solids, Phys. Rev. Lett. **118**, 087403 (2017).

[38] K. K. Hansen, T. Deffge, and D. Bauer, High-order harmonic generation in solid slabs beyond the single-active-electron approximation, Phys. Rev. A **96**, 053418 (2017).

[39] I. Floss, C. Lemell, G. Wachter, V. Smejkal, S. A. Sato, X.-M. Tong, K. Yabana, and J. Burgdörfer, Ab initio multiscale simulation of high-order harmonic generation in solids, Phys. Rev. A **97**, 011401(R) (2018).

[40] J. Li, S. Fu, H. Wang, X. Zhang, B. Ding, B. Hu, and H. Du, Limitations of the single-active-electron approximation in quantum simulations of solid high-order harmonic generation, Phys. Rev. A **98**, 043409 (2018).

[41] L.-J. Lü and X.-B. Bian, Multielectron interference of intraband harmonics in solids, Phys. Rev. B **100**, 214312 (2019).

[42] C. Yu, H. Iravani, and L. B. Madsen, Crystal-momentum-resolved contributions to multiple plateaus of high-order harmonic generation from band-gap materials, Phys. Rev. A **102**, 033105 (2020).

[43] X. Song, S. Yang, R. Zuo, T. Meier, and W. Yang, Enhanced high-order harmonic generation in semiconductors by excitation with multicolor pulses, Phys. Rev. A **101**, 033410 (2020).

[44] X. Liu, Y. Li, D. Liu, X. Zhu, X. Zhang, and P. Lu, Effects of quantum interferences among crystal-momentum-resolved electrons in solid high-order harmonic generation, Phys. Rev. A **103**, 033104 (2021).

[45] L. Yue and M. B. Gaarde, Expanded view of electron-hole recollisions in solid-state high-order harmonic generation: Full-brillouin-zone tunneling and imperfect recollisions, Phys. Rev. A **103**, 063105 (2021).

[46] H. G. Muller, Numerical simulation of high-order above-threshold-ionization enhancement in argon, Phys. Rev. A **60**, 1341 (1999).

[47] R. Kopold, W. Becker, M. Kleber, and G. G. Paulus, Channel-closing effects in high-order above-threshold ionization and high-order harmonic generation, J. Phys. B: At., Mol. Opt. Phys. **35**, 217 (2002).

[48] D. B. Milošević, E. Hasović, M. Busuladžić, A. Gazibegović-Busuladžić, and W. Becker, Intensity-dependent enhancements in high-order above-threshold ionization, Phys. Rev. A **76**, 053410 (2007).

[49] L. Xu and L. Fu, Multichannel Interference in Resonance-like Enhancement of High-Order Above-Threshold Ionization, Phys. Rev. Lett. **122**, 253202 (2019).

[50] E. S. Toma, P. Antoine, A. de Bohan, and H. G. Muller, Resonance-enhanced high-harmonic generation, J. Phys. B: At., Mol. Opt. Phys. **32**, 5843 (1999).

[51] D. B. Milošević and W. Becker, Role of long quantum orbits in high-order harmonic generation, Phys. Rev. A **66**, 063417 (2002).

[52] G. Vampa, C. R. McDonald, G. Orlando, D. D. Klug, P. B. Corkum, and T. Brabec, Theoretical Analysis of High-Harmonic Generation in Solids, Phys. Rev. Lett. **113**, 073901 (2014).

[53] G. Vampa, C. R. McDonald, G. Orlando, P. B. Corkum, and T. Brabec, Semiclassical analysis of high harmonic generation in bulk crystals, Phys. Rev. B **91**, 064302 (2015).

[54] K. Burnett, V. C. Reed, J. Cooper, and P. L. Knight, Calculation of the background emitted during high-harmonic generation, Phys. Rev. A **45**, 3347 (1992).

[55] A. D. Bandrauk, S. Chelkowski, D. J. Diestler, J. Manz, and K.-J. Yuan, Quantum simulation of high-order harmonic spectra of the hydrogen atom, Phys. Rev. A **79**, 023403 (2009).

[56] J. C. Baggesen and L. B. Madsen, On the dipole, velocity and acceleration forms in high-order harmonic generation from a single atom or molecule, J. Phys. B: At., Mol. Opt. Phys. **44**, 115601 (2011).

[57] D. Golde, T. Meier, and S. W. Koch, High harmonics generated in semiconductor nanostructures by the coupled dynamics of optical inter- and intraband excitations, Phys. Rev. B **77**, 075330 (2008).

[58] L. V. Keldysh, Ionization in the field of a strong electromagnetic wave, Zh. Eksp. Teor. Fiz. **47**, 1945 (1965) [JETP **20**, 1307 (1965)].

[59] M. Lewenstein, P. Balcou, M. Y. Ivanov, A. L'Huillier, and P. B. Corkum, Theory of high-harmonic generation by low-frequency laser fields, Phys. Rev. A **49**, 2117 (1994).

[60] L. Yue and M. B. Gaarde, Imperfect Recollisions in High-Harmonic Generation in Solids, Phys. Rev. Lett. **124**, 153204 (2020).

[61] L. Li, P. Lan, X. Zhu, and P. Lu, Huygens-Fresnel Picture for High Harmonic Generation in Solids, Phys. Rev. Lett. **127**, 223201 (2021).

[62] E. N. Osika, A. Chacón, L. Ortmann, N. Suárez, J. A. Pérez-Hernández, B. Szafran, M. F. Ciappina, F. Sols, A. S. Landsman, and M. Lewenstein, Wannier-Bloch Approach to Localization in High-Harmonics Generation in Solids, Phys. Rev. X **7**, 021017 (2017).

[63] X.-M. Tong and Shih-I Chu, Probing the spectral and temporal structures of high-order harmonic generation in intense laser pulses, Phys. Rev. A **61**, 021802(R) (2000).

[64] A. Zaïr, M. Holler, A. Guandalini, F. Schapper, J. Biegert, L. Gallmann, U. Keller, A. S. Wyatt, A. Monmayrant, I. A. Walmsley, E. Cormier, T. Auguste, J. P. Caumes, and P. Salières, Quantum Path Interferences in High-Order Harmonic Generation, Phys. Rev. Lett. **100**, 143902 (2008).

[65] H. K. Kelardeh, U. Saalmann, and J. M. Rost, Ultrashort laser-driven dynamics of massless dirac electrons generating valley polarization in graphene, Phys. Rev. Res. **4**, L022014 (2022).

[66] J. Guo, H. Zhong, B. Yan, Y. Chen, Y. Jiang, T.-f. Wang, J.-f. Shao, C.-b. Zheng, and X.-S. Liu, Comparison of high-order-harmonic generation on single-layer graphene flakes with armchair and zigzag types in an intense laser field, Phys. Rev. A **93**, 033806 (2016).

[67] D. B. Miloevi and W. Becker, Channel-closing effects in strong-field ionization by a bicircular field, J. Phys. B: At., Mol. Opt. Phys. **51**, 054001 (2018).

[68] R. Heather and H. Metiu, An efficient procedure for calculating the evolution of the wave function by fast Fourier transform methods for systems with spatially extended wave function and localized potential, J. Chem. Phys. **86**, 5009 (1987).

[69] S. Chelkowski and A. D. Bandrauk, Wave-function splitting technique for calculating above-threshold ionization electron spectra, Int. J. Quantum Chem. **60**, 1685 (1996).

[70] S. Chelkowski, C. Foisy, and A. D. Bandrauk, Electron-nuclear dynamics of multiphoton h_2^+ dissociative ionization in intense laser fields, Phys. Rev. A **57**, 1176 (1998).

[71] P. B. Corkum, Plasma Perspective on Strong Field Multiphoton Ionization, Phys. Rev. Lett. **71**, 1994 (1993).

[72] P. Salieres, B. Carre, L. Le Deroff, F. Grasbon, G. G. Paulus, H. Walther, R. Kopold, W. Becker, D. B. Milosevic, A. Sanpera, and M. Lewenstein, Feynman's path-integral approach for intense-laser-atom interactions, Science **292**, 902 (2001).

[73] A.-T. Le, H. Wei, C. Jin, and C. D. Lin, Strong-field approximation and its extension for high-order harmonic generation with mid-infrared lasers, J. Phys. B: At., Mol. Opt. Phys. **49**, 053001 (2016).

[74] M. S. Wismer, S. Y. Kruchinin, M. Ciappina, M. I. Stockman, and V. S. Yakovlev, Strong-Field Resonant Dynamics in Semiconductors, Phys. Rev. Lett. **116**, 197401 (2016).

[75] E. Blount, Formalisms of band theory, Solid State Phys. **13**, 305 (1962).

[76] S. Jiang, H. Wei, J. Chen, C. Yu, R. Lu, and C. D. Lin, Effect of transition dipole phase on high-order-harmonic generation in solid materials, Phys. Rev. A **96**, 053850 (2017).